BILINGUAL
PUBLISHING CO.
Pioneer of Global Academics Since 1984

Journal of Mechanical Materials and Mechanics Research

Volume 5 · Issue 1 · March 2022 | ISSN 2810-935X (Online)

BILINGUAL PUBLISHING CO.
Pioneer of Global Academics Since 1984

Editor-in-Chief

Dr. Jan Awrejcewicz
Lodz university of technology, Poland

Associate Editor

Dr. Kong Fah Tee
University of Greenwich, United Kingdom

Editorial Board Members

Farshad Abbasi,Iran
Venanzio Giannella,Italy
Mohamed Kamal Ahmed Ali ,Egypt
Hongping Hu ,China
Paweł Grzegorz Kossakowski,Poland
Jiusheng Bao,China
Mohamed El-Amine Slimani,Algeria
Ambreen Afsar Khan,Pakistan
Afshin Zeinedini,Iran
Jinglun Fu,China
Wuyi Wan,China
Salah Aguib,Algeria
Wei Cao,China
Hao Yi,China
Zhang Rongyun,China
Kishore Debnath,India
Marcos Rodriguez Millan,Spain
Nima Ahmadi,Iran
Bing Yang,China
Shahriar Dastjerdi,Iran
Vinothkumar Sivalingam,India
Saad AbdelHameed EL-Sayed,Egypt
XinJiang Lu,China
Sedat Yayla,Turkey
Artur Portela,Brazil
Arash Reza,Iran
Mohammad Nimafar,Iran
Xuejun Jason Liu,USA
Humaira Yasmin,Saudi Arabia
Daniele Cafolla,Italy
Abdelkader Doudou,Morocco
Elammaran Jayamani,Malaysia
Xikun Wang,China
Chew Kuew Wai,Malaysia
Yuan Kang,China
Kutsİ Savaş Erduran ,Turkey
Mohaned El wazziki,Canada
Lyudmila Ivanovna Gracheva,Ukraine
Milon Selvam Dennison,India
Khalil Ur Rehman,Pakistan
Ravinder Kumar,India
Samad Nadimi Bavil Oliaei ,Turkey
Zichen Deng,China
Samuel Filgueiras Rodrigues,Canada
Gadang Priyotomo,Indonesia
Ravindra Jilte,India
Alper Uysal,Turkey
Mehdi Safari,Iran
Matteo Strozzi,Italy
Asim Mukhopadhyay,India
Ahmad Jahanbakhshi,Iran
Dignesh Thesiya,India
Ahmed A. Hamoud,Yemen
Ali Abd El-Aty,Egypt

Volume 5 Issue 1 • March 2022 • ISSN 2810-935X (Online)

Journal of Mechanical Materials and Mechanics Research

Editor-in-Chief

Dr. Jan Awrejcewicz

BILINGUAL
PUBLISHING CO.
Pioneer of Global Academics Since 1984

BILINGUAL
PUBLISHING CO.
Pioneer of Global Academics Since 1984

Volume 5 | Issue 1 | March 2022 | Page1-39
Journal of Mechanical Materials and Mechanics Research

Contents

Editorial

Articles

BILINGUAL PUBLISHING CO.
Pioneer of Global Academics Since 1984

Journal of Mechanical Materials and Mechanics Research
https://ojs.bilpublishing.com/index.php/jmmmr

ARTICLE

Vacuum Filling Simulation with Combined Lagranian and VOF Method

Yujia Chen Maoxuan Cai Shixun Zhang Na Zhang Wei Cao[*]

National Engineering Research Center for Advanced Polymer Processing Technology, Zhengzhou University, Zhengzhou, Hennan, 450002, China

ARTICLE INFO

Article history
Received: 30 December 2021
Revised: 28 February 2022
Accepted: 21 March 2022
Published Online: 30 March 2022

Keywords:
Vacuum
Finite element method
Lagranian technique
VOF method
Flow front

ABSTRACT

Jetting succeeded by accumulation is the characteristic of the vacuum filling, which is different from the conventional pressure-driven flow. In order to simulate this kind of flow, a three-dimensional theoretical model in terms of incompressible and viscous flow is established, and an iterative method combined with finite element method (FEM) is proposed to solve the flow problem. The Lagranian-VOF method is constructed to trace the jetting and accumulated flow fronts. Based on the proposed model and algorithm, a simulation program is developed to predict the velocity, pressure, temperature, and advancement progress. To validate the model and algorithm, a visual experimental equipment for vacuum filling is designed and construted. The vacuum filling experiments with different viscous materials and negative pressures were conducted and compared with the corresponding simulations. The results show the flow front shape closely depends on the fluid viscosity and less relates to the vacuum pressure.

1. Introduction

Vacuum filling is an approach that uses vacuum to suck materials to fill the cavity. It is widely used in vacuum-assisted resin transfer molding (VARTM) and vacuum infusion molding process (VIMP). The most difficult issue is the prediction of complete fill time which closely depends on the fluid viscosity, density and vacuum. In order to simulate the process, scientists and engineers have developed some models and numerical methods to trace the flow advancement, calculate the values of physical variables and predict the filling time [1].

Using numerical simulation can predict the development and evolution of the flow front during the filling

---

*Corresponding Author:
Wei Cao,
National Engineering Research Center for Advanced Polymer Processing Technology, Zhengzhou University, Zhengzhou, Hennan, 450002, China;
Email: wcao@zzu.edu.cn

DOI: https://doi.org/10.30564/jmmmr.v5i1.4511

process, optimize the process and mold structure of composite molding [2], and improve the quality of parts [3,4]. Song and Youn [5] established an analytical model for the post-infusion VARTM process by the non-rigid control volume approach. They successfully predicted the thickness gradient due to the flexible nature of the bagging approach and the pressure gradient developed during infusion. It has also been used to predict the resin bleeding behavior for various processing scenarios. Robinson and Kosmatka [6] established compaction and permeability constitutive models, and proposed a numerical method to simulate the post-filling. Yang et al. [7] built the resin flow governing equations for vacuum-assisted resin infusion and an approach to calculate the primary flow by the normal Darcy's law. They conducted three examples to verify the precision and flexibility of the approach. Regarding resin as an incompressible fluid, Cai et al. [8] also used Darcy's law to describe the position of the resin flow front in the mold and the filling time, and used RTM-worx to complete the flow filling simulation.

There are two types of methods for advancement tracking, which are classified as Lagrangian and Eulerian [9]. The two methods are based on the strategies of mobile mesh and fixed mesh respectively. The Lagrangian method is limited by mesh deformation and contact processing [10]. To overcome this shortage it was developed into the arbitrary Lagrangian-Eulerian method which combines advantages of the two methods. Both Lagrangian and Eulerian methods have been employed to develop various frontier flow solutions. The well-known volume of filling (VOF) method and Level Set method are interface capture methods constructed under Eulerian mesh. They have strong topological processing ability and are widely used in the simulation of front flow. In 1981, hirt et al. [11] proposed VOF method. The VOF method can be divided into an algebraic VOF method and a geometric VOF method. The geometric VOF method geometrically reconstructs the free surface, and then uses the reconstructed free surface to update the volume fraction rate distribution. The algebraic VOF method solves the volume fraction rate transport equation directly, without involving any geometric object. Existing researches show that the VOF method can depict complex interface structure and changes, and can be applied to the solution of two-phase flow [12]. Gim et al. [13] presented an improved VOF model that based on smoothing functions, which effectively reduced the issue of spurious velocities. At present, most CFD programs use variations of the VOF method to solve the interfacial problems [14], which can be found in ANSYS Fluent, OpenFOAM, Gerris etc. Recently, Li et al. [15] developed a new calculation method via VOF method to predict the interface evolution, velocity and the temperature distribution. Fan et al. [16] also used this approach to design a new solver called varRhoTurbVOF based on OpenFOAM software to improve the turbulence models.

Osher and Sethian [17] developed the Level Set Method is another effective approach to predict flow front evolution developed in the 1980s. This method is widely used in many disciplines such as image processing, computational geometry, optimization and computational fluid dynamics. The basic idea of this method is to express the motion of the two-phase interface with the zero point of a higher-order function (Level Set function ϕ). The value of ϕ is used to distinguish the phases in the calculation area. Then update the interface by solving the advection equation of ϕ. The solution of ϕ may change greatly, therefore, it is necessary to reinitialize the function ϕ to maintain the distance function characteristics and the accuracy of the movement of the flow front [18,19]. Sussman et al. [20] proposed a method based on partial differential equations to reinitialize the level set function in 1994. To improve the simulated precision, Dai et al. [21] proposed a piecewise constant level set method for solving the topology optimization of steady NavierStokes flow. Sodeyama et al. [22] found that the choice of re-initialization method was very important to avoid non-physical deformation of ϕ and proposed a new re-initialization method to implement a multi-dimensional calculation of fluid flows. Furthermore, Hong et al. [23] established a new equidistant filling theory based on the level set function and a corresponding numerical algorithm based on the dynamic finite difference method. The algorithm can effectively produce the remanufacturing repair path of a complex die, and improve the efficiency of die manufacturing by more than 60%.

In this paper, a three-dimensional theoretical model for viscous flow driven by the vacuum is established and the finite element method is constructed to solve the flow problem. The Lagranian method is used to track the velocity, position and shape of the jet in the early stage. When the fluid reaches the bottom, the jet flow transfers to heaping and the backward filling happens under vacuum. The new development of the flow front is simulated by the VOF method. Based on the viscous flow theory and the Lagranian-VOF algorithm, a simulation program was developed to predict the velocity, pressure, temperature, and track the flow front and air trap position.

2. Vacuum Filling Theory and Numerical Method

2.1 Governing

The melt inertial force is much lower than the viscous force and is neglected. The governing equations for viscous, incompressible flow are written as

$$\nabla\cdot\mathbf{u} = 0\,, \tag{1}$$

$$\rho\mathbf{f} - \nabla p + \nabla\cdot\left(\eta\dot{\boldsymbol{\gamma}}\right) = \mathbf{0}\,. \tag{2}$$

Where ρ, C_p, k and η are the melt density, specific heat, thermal conductivity and viscosity respectively, and $\rho\mathbf{f}$, $\mathbf{u}$, p and $\dot{\boldsymbol{\gamma}} = \left(\nabla\mathbf{u} + \nabla\mathbf{u}^T\right)/2$ represent the body force, velocity, pressure and shear rate tensor respectively.

2.2 Boundary Conditions

The pressure are assumed to be atmosphere and vacuum at the gate and meltfront respectively

$$p = p_a \quad \text{at meltfront,} \tag{3}$$

$$p = p_v \quad \text{at meltfront.} \tag{4}$$

2.3 Numerical Method

Let Ω_t denote the filled region at current time t and $H^i\left(\Omega_t\right)$ represents the ith order Hilbert function space in region Ω_t. Multiplying the governing equations with test functions $\left(q,\mathbf{v}\right)\in H^1\left(\Omega_t\right)\times H^2\left(\Omega_t\right)^3$ and integrating by parts using the Gauss formula subject to the boundary conditions (3) and (4) yields the variational equations

$$\iiint_{\Omega_t} \mathbf{u}\cdot\nabla q d\Omega = \iint_{\partial\Omega_t} \mathbf{u}_n dS \qquad \forall q\in H^1\left(\Omega_t\right), \tag{5}$$

$$\iiint_{\Omega_t} \eta\left(\nabla\mathbf{u} + \left(\nabla\mathbf{u}\right)^T\right):\nabla\mathbf{v}d\Omega + \iiint_{\Omega_t}\nabla p\cdot\mathbf{v}d\Omega - \iiint_{\Omega_t}\rho\mathbf{f}\cdot\mathbf{v}d\Omega = 0. \tag{6}$$

We use the Galerkin finite element method to discretize the variational Equations (5) - (6). The part is discretized with tetrahedral elements, and the velocity **u** is approximated with $P_2^{(10)}$ quadratic polynomials (10 nodes) owing to their second-order derivatives in the equations. The pressure p is approximated with $P_1^{(4)}$ linear polynomials (4 nodes). This interpolation satisfies the Brezzi-Babuska condition for numerical stability.

The pressure, velocity are interdependent in the above equations. To determine the two variables simultaneously, the time step and mesh sizes have to be satisfied the strict limitation to ensure numerical stability and convergence. Sometimes this requires a very small time step and fine mesh which involves a large number of computations. However, if the pressure is assumed to be known, then a nominal solution for velocity can be obtained from the invariant momentum Equation (6) at node P.

$$a_P^{\mathbf{u}}\mathbf{u}_P + \sum_N a_N^{\mathbf{u}}\mathbf{u}_N = -\sum_E c_E\left(\nabla p\right)_E\,. \tag{7}$$

Here N and E denote the nodes and elements surrounding node P respectively. Substituting this formula into the invariant continuity Equation (5) yields

$$\iiint_{\Omega_t} c'\nabla p\cdot\nabla q d\Omega = Q \qquad \forall q\in H^1\left(\Omega_t\right) \tag{8}$$

Equation (8) is the weak form of pseudo Poisson equation for pressure p, which makes the discrete matrix symmetric. This increases the convergence of the iterative scheme for solving linear equations, such as in the Gauss-Seidel method. When the pressure is determined the velocity can be calculated by Equation (7).

2.4 Fluid Advancing Simulation

The fluid used for vacuum is usually less viscous material, which leads the fluid filling like pillar flow. When the pillar arrives the bottom or contacts with the early arrived fluid , it piles along the opposite direction of gravity. The fluid advances with different manners in the two stages.

In order to trace the fluid advancement in pillar flow correctly, the Lagrange method is employed to calculate the flow fields and determine the fluid advancement. Assume a particle identified with **X** enters the cavity, its new position can be calculated with the following formula in Lagrange expression

$$\frac{d\mathbf{X}}{dt} = \mathbf{u}\,. \tag{9}$$

The velocity **u** is determined from governing equations, and the new position of the particle can be calculated with integration of Equation (9).

When the fluid switches to piled filling stage, the gravity drives the fluid to fill the remain cavity while restricted by the viscous force. The advancement is similar with viscous fluid filling droved by pressure. So the conventional volume of filling (VOF) approach is employed to predict the fluid advancement. Let F represents the filled factor of a control volume, it must satisfy the transport equation

$$\frac{\partial F}{\partial t} + \mathbf{u}\cdot\nabla F = 0\,. \tag{10}$$

In the first filling stage, the velocity of the particle decreases significantly once contacts with the previous arrived fluid while the viscous force increases obviously. So the velocity and viscous stress derivatives are used as the critical values switch from pillar filling to fluid advancing.

3. Experiment Setting

3.1 Experimental Equipment and Materials

The vacuum filling equipment is consisted by vacuum pump, buffer barrel, vacuum filling container and material container, see Figure 1. The buffering barrel is used to store the suction fluid to prevent backward fluid into the pump. The experimental equipment is connected by rubber hose. The volume of the glass cup is a 300 mL, and both the suction fluid tube diameter and extraction air tube diameter are both 10 mm. Once the vacuum pump starts the fluid in the beaker will be sucked into the glass cup, and stop when the power turns off.

The flow front of the vacuum filling is recorded by video. The mixture of resin GE-7118A and curing agent GE-7114B was first used in the experiment. They are mixed at room temperature of about 20 °C, and the mass ratio of the two materials is 100:30. The vacuum filling was first performed at minus 0.75 atm and get the filling front by video, see Figure 2(a). In order to change the fluid viscosity rapidly some soil is also added to this mixture. The filling front is shown in Figure 2(b). The fluid starts accumulating along the petting pillar when the viscosity increases.

3.2 Improvement of Experiments

The shortage of the experiment is the flow front cannot be well captured by the camera especially for the first mixture, and the liquid column was obviously inclined. In addition, the bubbles appearing in the fluid during the experiments, which influences fluid advancing.

To improve the imagine resolution, the hair conditioner was used for experiments instead of the mixture of resin GE-7118A and curing agent GE-7114B. In order to prevent bubbles during the filling the material was drained in drying hopper at room temperature. In addition, the pipe angle was adjusted so as to the jetting column is vertical to the bottom. The flow fronts are shown in Figure 3 after improving. It can be seen that the problem of tilt jetting column had been significantly improved. The bubble and delamination phenomenon had also been removed.

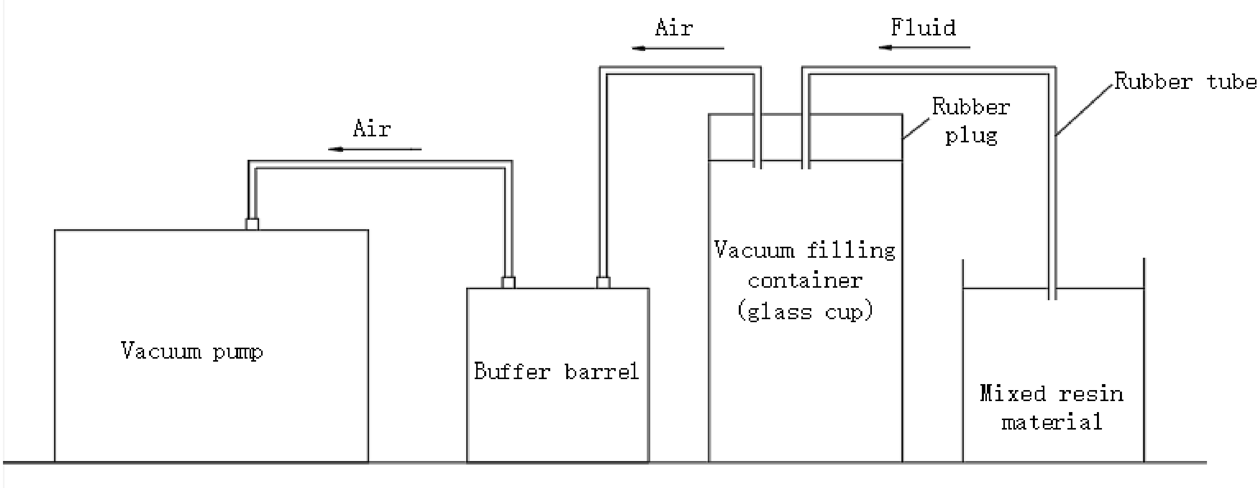

Figure 1. The schematic diagram of the vacuum equipment

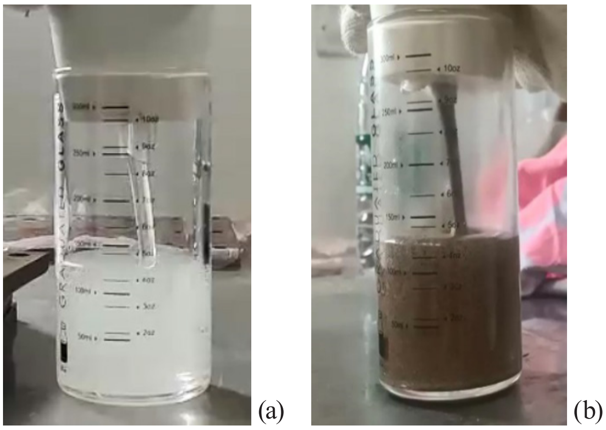
(a) (b)

Figure 2. Screenshot of the vacuum filling at 1s for (a) mixture of resin and (b) mixture with additional soil.

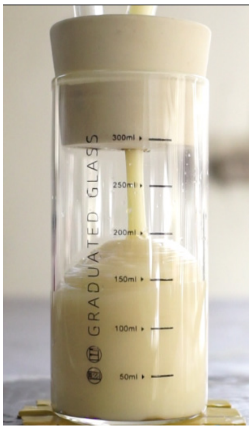

Figure 3. The vacuum filling with hair conditioner.

4. Results and Discussion

To perform the numerical simulation, the container, see Figure 4, was discretized into 78910 tetrahedral elements. The temperature was set to ambient temperature 20 °C and the gravity direction is vertical the ground. We change the material viscosity and negative pressure to validate the proposed method.

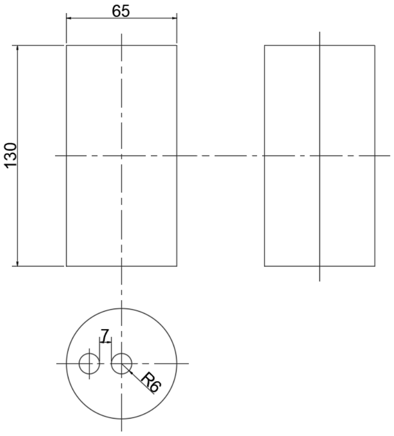

Figure 4. Schematic diagram of glass cup.

4.1 Viscosity Effects

The vacuum filling was firstly conducted at 1 minus atm. When the fluid enters the glass under negative pressure, it is almost equivalent to that the fluid is only affected by gravity. When the temperature does not change, the viscosity of the mixture will keep constant. The fluid does not accumulate along the jetting column and there is a slight depression near the liquid column as the viscosity is only 350 mPa·s which can not sustain the accumulated materials. We used analysis software to simulate the vacuum filling of resin mixture. The experimental and simulated fluid advancements at 1 s and 2 s are shown in Figures 5(a) and 5(b) respectively. The simulated fluid advancements are in good agreement with the experimental results. Figure 5 shows the program is also capable of simulation of the depression in low viscous vacuum.

Then some soil was added to resin to increase the material viscosity and conducted the vacuum filling again. The fluid advancements corresponding to 1 s and 2 s are shown in Figures 6(a) and 6(b). The viscosity of the sample in the experiment increases to 2500 mPa·s. The filling volume within the same period is smaller than that

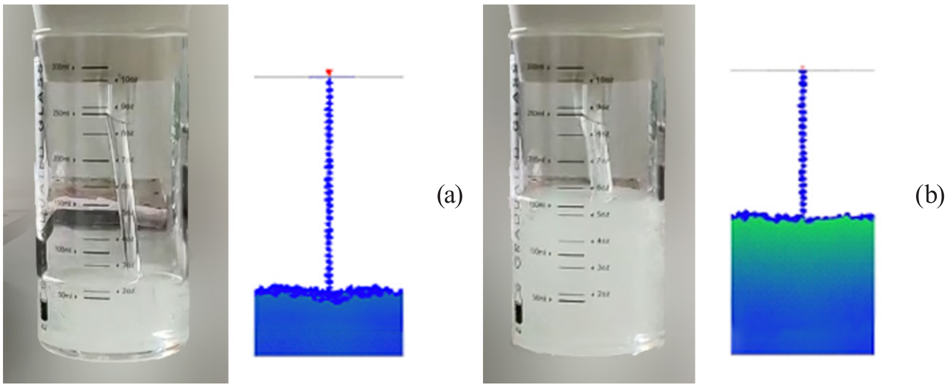

Figure 5. Comparison between experimental and simulated vacuum filling advancements at (a) 1 s and (b) 2 s under minus 1 atmosphere.

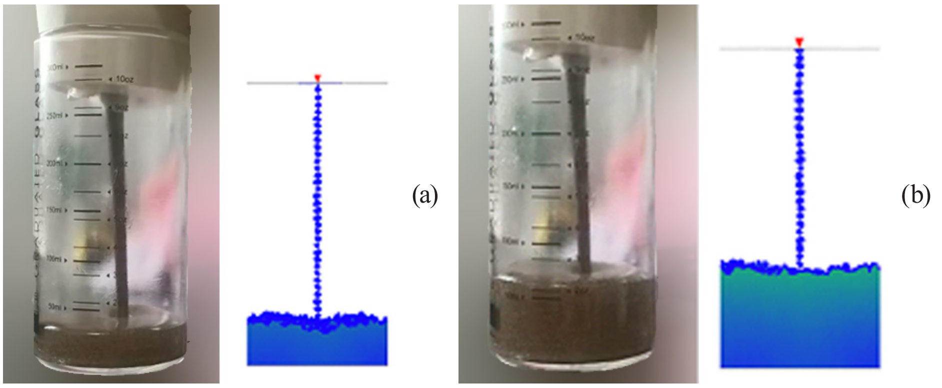

Figure 6. Comparison of experimental and simulated filling advancements of mixed resin and soil at (a) 1 s and (b) 2 s under minus 1 atmosphere

of the previous one. This is because the flow resistance increases with the enhance of fluid viscosity. Both the experimental and simulating results show that the middle depression near the liquid column still exists but shallower than before. The accumulated pyramid shape along the jetting column does not happen during the whole vacuum filling for the two materials. This mean the shape of front advancements depends on the fluid viscosity and does not change significantly for this viscosity scale.

Figure 5 and Figure 6 indicate the filling speed, front shape and accumulation along the jetting pillar depend on the material viscosity. To verify this assumption, we further increased the material viscosity to 9600 mPa·s by replaced the material with hair conditioner. In addition, we have also improved the program so that the jetting column is displayed with runner elements instead of triangle elements. The experimental and simulated front advancements are shown in Figure 7.

Figure 7 shows the filled volumes are further reduced due to increased viscosity. The filling velocity is different from that of low viscosity fluid in the first stage of filling. In the initial stage of filling, it can be observed that the time taken for high viscosity fluid to enter from the inlet to the cup of the glass increases compared with low viscosity fluid. Through the recording of the camera, we found that the low viscosity fluid took 130 millisecond. However, high viscosity fluids took 197 millisecond. In addition, the flow front shape is much different from that of low viscous fluid. The pyramid shape generates in the middle front area for high viscous fluid filling. It maintains its shape and quickly spreads around and fills the whole glass. Fortunately the developed program successfully predicts this phenomenon as we considered all the fundamental factors especially viscous force in the theoretical model. In addition, the program can predict the front heights accurately, which means the program can also work well for high viscous fluid.

4.2 Negative Pressure Effects

The vacuum pressure was reduced to minus 0.75 atm. and conducted the experiment and simulation again with the soil mixture. The filling advancements corresponding to 1 s and 2 s are shown in Figures 8(a) and 8(b). The filling volumes are only half of minus 1 atm within the same

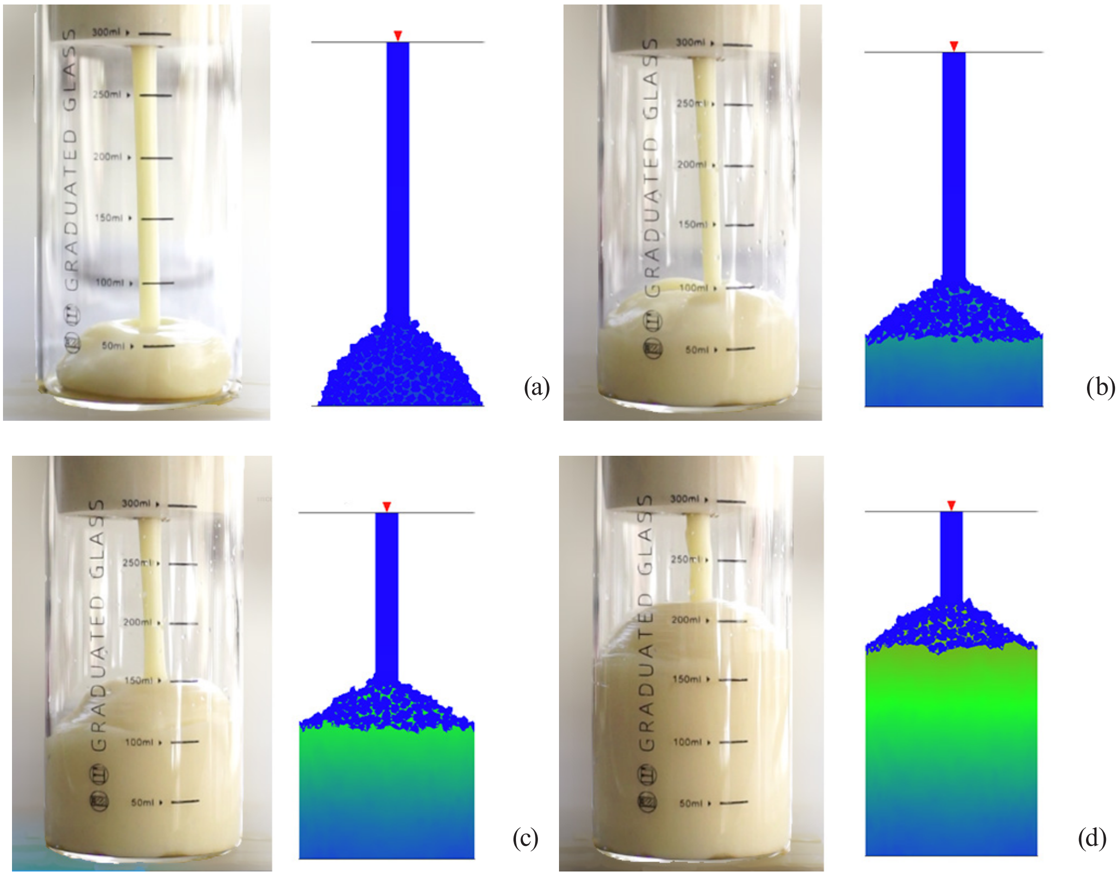

Figure 7. Comparison of the experimental and simulated filling front shapes for (a) 1 s, (b) 2 s, (c) 3 s and (d) 4 s under minus 1 atmosphere.

filling period. The flow front shapes are consistent with the before though the vacuum pressure changes. Meanwhile, Figure 6 and Figure 8 show the diameters of the jetting column do not vary with vacuum pressure, which indicates the jetting shape only depends on the entrance diameter and less relates the pressure.

Similarly, we also conducted comparative experiments with high viscosity materials at the same pressure. The results are shown in Figure 9. Both experimental and simulated results illustrate that the shape of the flow front does not change much, and they are almost the same with the high vacuum one. Therefore, it once again demonstrates that the filling shape only depends on the fluid viscosity and less relate the value of vacuum which only affect the filling speed.

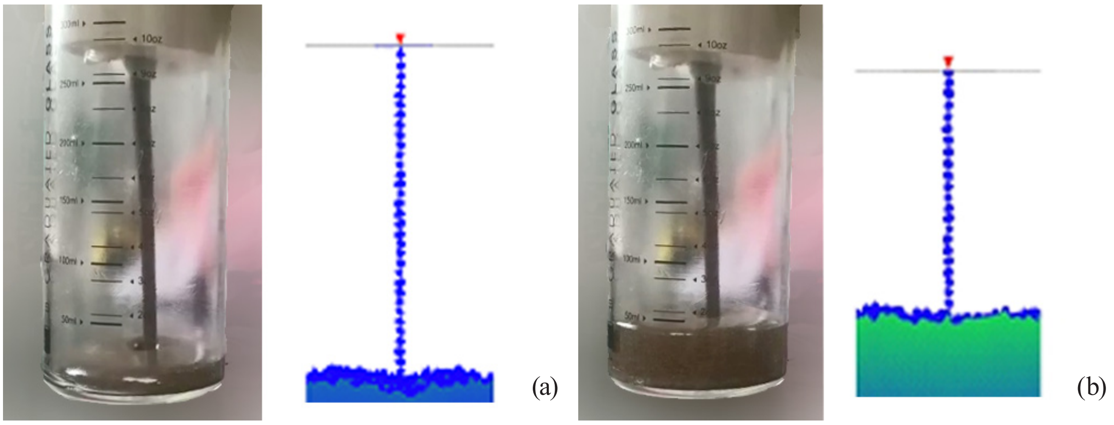

Figure 8. Comparison of experimental and simulated fluid advancements of mixed resin and soil at (a) 1 s and (b) 2 s under minus 0.75 atmosphere.

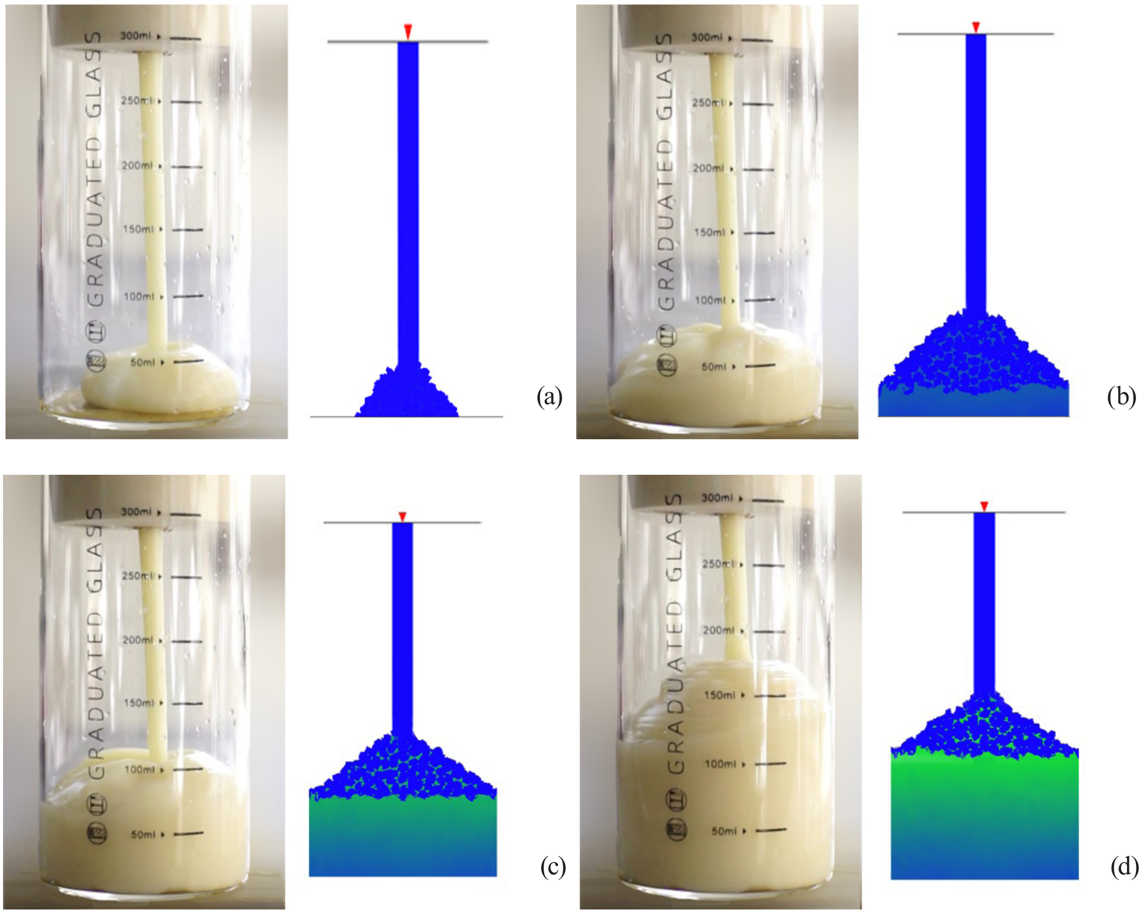

Figure 9. Comparison of the experimental and simulated filling front shapes for (a) 1 s, (b) 2 s, (c) 3 s and (d) 4 s under minus 0.75 atmosphere.

5. Conclusions

The vacuum filling is considerably different from the fluid filling of pressure-driven flow, in which the gravity force plays an important role. The conventional VOF method can not be used to simulate the flow front. In order to predict the filling process accurately a flow model is established to describe the viscous fluid. An iterative method combined with FEM is proposed to solve the flow problem. In order to capture the flow front mixed with jetting and accumulation a Lagranian and VOF method is constructed to simulate the advancement. A series of vacuum filling experiments were conducted to validate the model and numerical methods. The results of this study show:

(a) The flow front shape closely depends on the fluid viscosity and less relates to the vacuum pressure.

(b) The depression on the middle area will be formed for the low viscous fluid vacuum filling.

(c) The pyramid front generates for high viscous fluid vacuum filling as the larger viscous material can bear heavy force.

Acknowledgements

Financial supports from the National Science Foundation of China (No. 11672271), and Shenzhen Zhaowei Machinery & Electronics CO., LTD. (No. 20210035A and 20210035B) for this research work are gratefully acknowledged.

Conflict of Interest

The authors do not have any possible conflicts of interest.

References

[1] Rodríguez-González, P., Robles Valero, P.E., Fernández-Abia, A.I., et al. (2020). Application of vacuum techniques in shell moulds produced by additive manufacturing. Metals. 10(8), 1-20.
DOI: https://doi.org/10.3390/met10081090

[2] Sorgato, M., Babenko, M., Lucchetta, G., et al., 2017. Investigation of the influence of vacuum venting on mould surface temperature in micro injection moulding. International Journal of Advanced Manufacturing Technology. 88(1-4), 547-555.
DOI: https://doi.org/10.1007/s00170-016-8789-8

[3] Xiao, L., Huang, J., Dai, Y.C., et al., 2010. Rapid fabrication of micro-gear via vacuum casting technique of silicone rubber mould. Advanced Materials Research. 97-101, 4016-4019. www.scientific.net/AMR.97-101.4016” TARGET=”_blank”>
DOI: https://doi.org/10.4028/www.scientific.net/AMR.97-101.4016

[4] Kuo, C., Liu, H., Chang, C., 2020. Optimization of vacuum casting process parameters to enhance tensile strength of components using design of experiments approach. International Journal of Advanced Manufacturing Technology. 106(9-10), 3775-3785.
DOI: https://doi.org/10.1007/s00170-019-04905-6

[5] Song, Y.S., Youn, J.R., 2009. Numerical investigation on flow through porous media in the post-infusion process. Polymer Composites. 30(8), 1125-1131.
DOI: https://doi.org/10.1002/pc.20668

[6] Robinson, M.J., Kosmatka, J.B., 2014. Analysis of the post-filling phase of the vacuum-assisted resin transfer molding process. Journal of Composite Materials. 48(13), 1547-1559.
DOI: https://doi.org/10.1177/0021998313488150

[7] Yang, B., Jin, T., Bi, F., et al., 2014. Modeling the resin flow and numerical simulation of the filling stage for vacuum-assisted resin infusion process. Journal of Reinforced Plastics and Composites. 33(21), 1976-1992.
DOI: https://doi.org/10.1177/0731684414551039

[8] Cai, Y.Q., Chen, Q.L., Zhu, Z.Y., et al., 2018. Study on VARI Process Parameters of Fiber Composites. China Plastics Industry. 46(07), 46-50. (in Chinese).

[9] Shen, C.Y., Ren, M.K., Liu, C.T., et al., 2020. A review on the theories and numerical methods for injection molding simulations. Scientia Sinica Technologica. 50(06), 667-692. (in Chinese).

[10] Choi, D., Lee, S., Im, Y., 2005. Fringe element reconstruction for front tracking for three-dimensional incompressible flow analysis. International Journal for Numerical Methods in Fluids. 48(6), 631-648.
DOI: https://doi.org/10.1002/fld.943

[11] Hirt, C.W., Nichols, B.D., 1981. Volume of fluid (VOF) method for the dynamics of free boundaries. Journal of Computational Physics. 39(1), 201-225.
DOI: https://doi.org/10.1016/0021-9991(81)90145-5

[12] Arai, E., Villafranco, D., Grace, S., et al., 2020. Simulating bubble dynamics in a buoyant system. International Journal for Numerical Methods in Fluids. 92(3), 169-188.
DOI: https://doi.org/10.1002/fld.4778

[13] Soh, G.Y., Yeoh, G.H., Timchenko, V., 2016. Improved volume-of-fluid (VOF) model for predictions of velocity fields and droplet lengths in microchannels. Flow Measurement and Instrumentation. 51, 105-115.
DOI: https://doi.org/10.1016/j.flowmeasinst.2016.09.004

[14] Roenby, J., Bredmose, H., Jasak, H., 2016. A compu-

tational method for sharp interface advection. Royal Society Open Science. 3(11), 160405-160405.
DOI: https://doi.org/10.1098/rsos.160405

[15] Li, F., Zhao, H., Ren, F., et al., 2020. Simulations and experiments of mould filling in lost foam casting. International Journal of Cast Metals Research. 33(4-5), 194-200.
DOI: https://doi.org/10.1080/13640461.2020.1822572

[16] Fan, W., Anglart, H., 2020. varRhoTurbVOF: A new set of volume of fluid solvers for turbulent isothermal multiphase flows in OpenFOAM. Computer Physics Communications. 247, 106876.
DOI: https://doi.org/10.1016/j.cpc.2019.106876

[17] Osher, S., Sethian, J.A., 1988. Fronts propagating with curvature-dependent speed: Algorithms based on hamilton-jacobi formulations. Journal of Computational Physics. 79(1), 12-49.
DOI: https://doi.org/10.1016/0021-9991(88)90002-2

[18] Ngo, L.C., Choi, H.G., 2016. A local level set method based on a finite element method for unstructured meshes. Journal of Mechanical Science and Technology. 30(12), 5539-5545.
DOI: https://doi.org/10.1007/s12206-016-1122-5

[19] Ngo, L.C., Choi, H.G., 2017. Efficient direct re-initialization approach of a level set method for unstructured meshes. Computers & Fluids. 154, 167-183.
DOI: https://doi.org/10.1016/j.compfluid.2017.06.002

[20] Sussman, M., 1994. A level set approach for computing solutions to incompressible two-phase flow. Journal of Computational Physics. 114(1), 146-159.
DOI: https://doi.org/10.1006/jcph.1994.1155

[21] Dai, X., Zhang, C., Zhang, Y., et al., 2017;2018. Topology optimization of steady navier-stokes flow via a piecewise constant level set method. Structural and Multidisciplinary Optimization. 57(6), 2193-2203.
DOI: https://doi.org/10.1007/s00158-017-1850-x

[22] Sodeyama, K., Yoshino, H., Ohta, M., et al., 2020. Application of a level-set method for deposition of fine particles on a filter. Kagaku Kōgaku Ronbunshū. 46(3), 49-56.
DOI: https://doi.org/10.1252/kakoronbunshu.46.49

[23] Hong, X., Xiao, G., Zhang, Y., et al., 2021;2022. A new path planning strategy based on level set function for layered fabrication processes. International Journal of Advanced Manufacturing Technology. 119(1-2), 517-529.
DOI: https://doi.org/10.1007/s00170-021-08239-0

BILINGUAL PUBLISHING CO.
Pioneer of Global Academics Since 1984

Journal of Mechanical Materials and Mechanics Research
https://ojs.bilpublishing.com/index.php/jmmmr

ARTICLE

Study of Concrete Filled Unplasticized Poly-Vinyl Chloride Tubes as Columns under Axial Loading

Manish Sharma* **Md. Imteyaz Ansari** **Nazrul Islam**

Department of Civil Engineering, Faculty of Engineering and Technology, Jamia Millia Islamia, New Delhi, 110025, India

ARTICLE INFO

Article history
Received: 7 March 2022
Revised: 12 April 2022
Accepted: 22 April 2022
Published Online: 29 April 2022

Keywords:
Unplasticized Poly-Vinyl Chloride (UPVC) tubes
Composite column
Tube confinement
Column strength

ABSTRACT

This article aims to examine the behavior of Unplasticized Poly-Vinyl-Chloride (UPVC) bounded reinforced columns with polypropylene fibers under axial compression. To develop this model, samples of concrete filled UPVC pipe (CFUT) with different geometric properties were tested. To obtain the specimens different class pipes with three different diameters were used to investigate the sensitivity of these columns to various parameters. The effect of each variable on the ultimate strength, ductility and confinement efficiency of the samples was investigated. All specimens were compressed by applying load only to the concrete core to obtain the load-displacement variations and the corresponding deformation mode. A finite element model was developed using the proposed stress-strain variation of confined concrete with UPVC tubes to simulate axial compression of CFUT specimens. According to the results obtained, the effect of the change in diameter-thickness ratio failure stress of concrete limited by (D/t) is obtained and discussed with empirical relationship. Polypropylene fibers were found to slightly increase column strength up to a certain volume fraction, after which the strength generally experienced a decrease.

1. Introduction

Concrete filled tube is a type of composite column that consists of a tubular encasing of any shape with concrete filled into it. The tube may be made up of different material like steel, fibre reinforced plastic (FRP) and Poly Vinyl Chloride (PVC)/Unplasticised PVC. Plastics have outstanding properties such as low cost, high resistance to severe environmental attack and high strength-to-weight ratio. Because of these properties, plastics used for different purposes, including commercial and engineering. UPVC pipes are often used for worldwide water supply. These pipes are designed for the induced internal pressure of the flowing water. These pipes are divided into different classes on the basis of resistance to water pressure and depending on the nominal pressure exerted by the flowing water.

Yu et al. [1] performed investigations on the CFRPPVC confined long and short columns under cyclic displacements and determined the failure mechanisms and the general performance. Gao et al. [2] performed experimental and

---

*Corresponding Author:
Manish Sharma,
Department of Civil Engineering, Faculty of Engineering and Technology, Jamia Millia Islamia, New Delhi, 110025, India;
Email: smanish337@gmail.com

DOI: https://doi.org/10.30564/jmmmr.v5i1.4494

numerical studies on the recycled aggregate concrete confined with PVCPFRP tube. Studies have been performed on plain concrete-encased with PVC tubes to measure the axial load and deformation characteristics [3]. Wang and Yang [4] studied the effects of material mechanical parameters of PVC-confined plain concrete and proposed a simple relation to calculate the increase in load capacity due to PVC confinement. Wang et al. [5] validated a finite element (FE) model for a wide range of experimental concrete-filled steel columns and used it to generate parameter variance in over 499 circular and rectangular stub columns. The parameters included steel tube yield strength, concrete core compressive strength, diameter-to-thickness ratio (for circular stubs), height-to-width ratio and height-to-thickness ratio (for rectangular columns). They subsequently proposed regression models for the prediction of compressive strength, stiffness, and deformation of the composite columns. Saadoon [6] to study parameters such as concrete strength, tube thickness and slenderness ratio. Saadoon also investigated the effect of transverse steel reinforcement in these PVC confined columns. An important characteristic of the thermoplastic family is its durability against harsh and undesirable environments, where exposed concrete or steel would deteriorate quickly. Machine Hsie et al. [7] studied the combined effects of two types of PP fibers and observed an increase in compressive strength as high as 17%. An investigation with scanning electron microscope (SEM) was performed by Sun and Xu [8] and it was observed that PP fibers cause widespread alteration in the microstructure of concrete, and therefore have positive effects on various mechanical properties of concrete. Gupta and Verma [9] immersed a series of samples of varying diameter-thickness and length-thickness in artificial seawater and then tested them under axial compression to examine the coating effectiveness of PVC pipes in the marine environment. No significant difference in sample response was observed and it was concluded that the PVC coating effectively protected the concrete. Wang and Yang [10] presented an experimental study on plastic pipe wrapped concrete (PPC). Plastic pipes are taken as HDPE pipes. They reported that the thickness and unconfined compressive strength of the concrete affect the ultimate strength and post-peak behavior of the PPC. They observed that at the lower constraint, the breaking mode was shear, and at the higher constraint, the drum type. According to Ragab et al. [11] tested rigid PVC pipes with a diameter of 60 mm (2.36 inches) and biaxially 5.3 mm (2.09 inches) thickness with 1 MPa (145 psi) working pressure. The tension system covering the four quadrants of the plane-stress space. Upload done tension, compression, torque, and internal and external pressure. They tested the samples at different strain rates and temperatures. They planned yield's location various strain rates and temperatures. They observed that rigid PVC pipes followed the von Mises criterion. A study with scanning electron microscopy (SEM) was conducted by Sun and Xu [12] and it has been observed that PP fibers cause widespread changes in the microstructure of concrete and therefore have positive effects on various mechanical properties of concrete.

Based on the above discussion, composite use of PVC and concrete addresses some important mechanical and environmental challenges. In addition to the advantages of UPVC pipes such as no mold demand, fast construction, chemical and mechanical improvements due to mechanical protection and containment for core concrete.

It can be seen that only a few researchers have studied the behavior of concrete-filled plastic pipes subjected to axial compression. The investigation of such columns with the help of computer modeling is still not reported. In this study, a systematic experimental and computational study is attempted to understand and model the behavior of concrete filled PVC pipes subjected to axial compression.

2. Experimental Study

2.1 Specimen Configuration

Column specimens were manufactured and tested under axial compression applying only on concrete core. CFUT specimen is made with tube of different class having different nominal diameter filled with plain concrete of grade M30 & M40. The pipes are placed in the circular mold before casting the samples. Freshly prepared concrete was placed in three layers and appropriate vibration and compression have been made in each layer. The samples were tightly covered with a thick polyethylene sheet to avoid evaporation of water. So sample identificated as 200P5PC40; where 200 indicates the outer diameter of the pipe, PC40 is that the plain concrete of grade M40, P5 is used for class 5 pipe with nominal pressure of 1.0 MPa. These specimens and their corresponding parameters are listed in Table 1 and Table 2, respectively. D is the outer diameter (including the pipe thickness), h is the height of the specimen, and t is the thickness of pipe.

2.2 Material Properties

2.2.1 Concrete

Samples are made of Ordinary Portland cement, fine and coarse aggregates and admixture with mix designs of M30 & M40. Superplasticizer was added as a percentage of cement weight to increase the workability of the samples and increase their strength by reducing the water content. Concrete mix proportions are listed in Table 1.

Table 1. Concrete Mix proportions used in this study

Grade	M30	M40
w/c ratio	0.45	0.40
Water (kg/m^3)	171	160
Cement (kg/m^3)	380	400
Fine Aggregate (kg/m^3)	673	675
Coarse Aggregate (kg/m^3)	1089	1093
Admixture (%)	0.25	0.35
Cube strength (MPa)	42.22	48.88

2.2.2 Unplasticized Poly-Vinyl Chloride (UPVC) Tubes

Unplasticized Polyvinyl Chloride is a hard form of PVC (a type of plastic) which used especially for making pipes and window frames. Although some researchers use the terms PVC and UPVC interchangeably, their industrial definitions are quite different and exhibit different mechanical properties. PVC is often used to make siding and fences, whereas UPVC is used for window and door construction. UPVC is a durable material. It does not contain phthalates or BPA. It provides a safe local product. It is also highly resistant to corrosion, weathering, and chemicals. The use of PVC in confinement of concrete specimens is investigated to some extent in the literature. Due to these desirable characteristics, this study attempts to evaluate the enhancement behavior of columns confined with UPVC tubes.

Different classes of pipes are usually specified with the maximum nominal pressure procured from the market. These UPVC pipes of class 3, 4 and 5 with nominal pressure of 0.6 MPa, 0.8 MPa and 1.0 MPa and the diameters of 160 mm, 200 mm and 225 mm used in this study. The specimen length of 800 mm made by this different class of UPVC Pipes. The authors conducted a series of tests to determine the mechanical properties of the UPVC tube. To determine the tensile behaviour of the UPVC, standard specimens (Figure 1) were extracted from pipes. The material properties of the UPVC element were determined in accordance with the tension test of the UPVC specimen shown in Figure 2, and the stress-strain curve of UPVC is shown in Figure 3, which finds an ultimate tensile stress of approximately 52 MPa at 20 °C.

Figure 1. Specimen

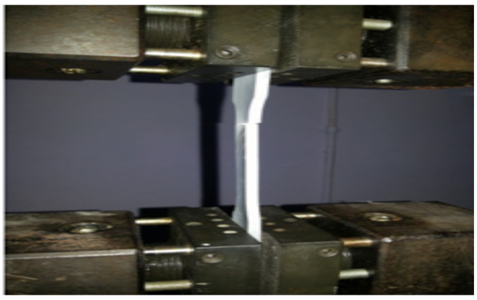

Figure 2. Tension test of UPVC

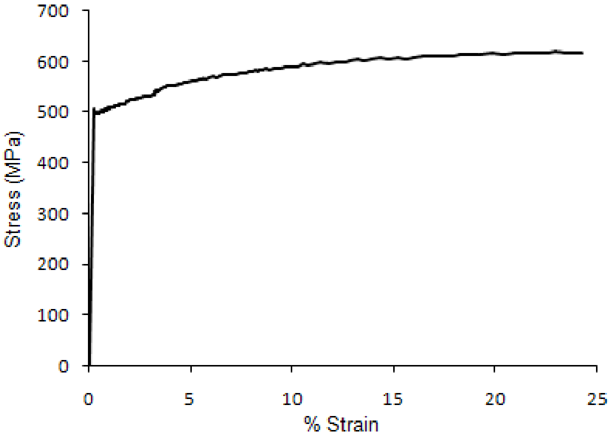

Figure 3. Stress-strain curve of UPVC

Table 2 summarizes the mechanical properties of the UPVC pipes that were provided in the manufacturer's, such as young's modulus, density and Poisson's ratio. Internal hydrostatic pressure test of UPVC pipes was conducted in the laboratory to get confining pressure. It's set up shown in Figure 4 and the confining pressure is given in Table 3.

Table 2. Physical properties of UPVC provided by the manufacturer

Characteristics	Value
Density	1.3 gm/cm^3
Elastic modulus	880 MPa
Ultimate tensile strength	22.5 MPa
Poisson's ratio	0.35
Service life	>50 years

2.3 Test Setup and Apparatus

The test was performed using a servo-hydraulic Universal Testing Machine (UTM) with a loading capacity of 25000 KN. Template testing and setup tools are shown in

Table 3. Confining pressure of UPVC pipes tested by the authors

Class of pipe (Nominal pressure)	Dimensions (mm)			Confining pressure (MPa)	
	Nominal Outer diameter (D)	Internal diameter (d)	Thickness (t)	Experimental	Calculated p= *fu(2t/d)*
Three (0.6 MPa)	160	152.17	3.99	1.15	1.18
	200	187.97	5.22	1.35	1.42
	225	207.48	7.02	1.72	1.87
Four (0.8 MPa)	160	149.44	5.94	1.52	1.57
	200	183.34	8.11	1.99	1.99
	225	205.42	8.89	2.00	2.09
Five (1.0 MPa)	160	146.15	8.65	2.15	2.16
	200	181.44	9.58	2.25	2.20
	225	204.59	9.97	2.17	2.19

Figure 4. set up for find confining pressure

Figure 5. It is noteworthy that capping is done precisely to produce a thin layer. All column models were loaded with a displacement control rate of 0.4 mm/min until they reached approximately 1.2%-2.5% strain. Although some of these closed models can often be overcrowded, testing has been discontinued following a significant reduction in load capacity. The displacement used only concrete. Tubes were used only for confinement purpose. Deformation was recorded from 2 LVDTs placed on opposite sides of the crossheads to record the entire length of the samples. The load-displacement curves were recorded by the machine automatically.

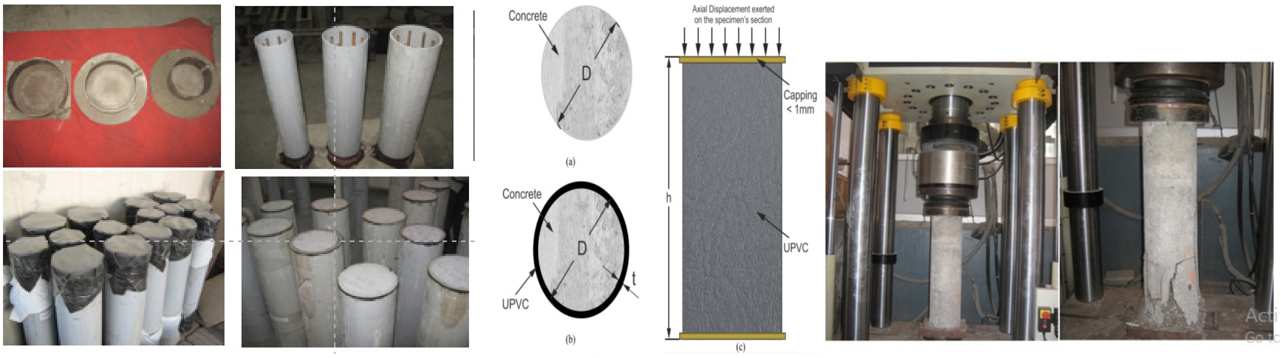

Figure 5. Casting & Testing of specimens

3. FEM Modelling and Simulation

FEM feature 3D model was developed using Abaqus software to mimic a concrete filled UPVC tube under axial pressure. For modeling a concrete core, three dimensions eight solid elements of node "SOLID 65" were used. To model tube, an eight-node solid element SOLID 45 was used. The main reinforcement and the lateral relationships are modeled by the link element "LINK8" [15]. A discrete model was used to model vertical steel. Bangash [13] unconfined concrete model was found to be suitable for modelling concrete in RCC. Contact is defined as a surface contact. The yield stress of the plate is taken as 1000 MPa. The stress-strain variation is modeled using the elastic-perfect plastic material command. The plate behaved as rigid. The mesh size was chosen from 4 mm to 8 mm for the tube, concrete core and steel plate. Load was applied to the column through the top loading plate. Surface contact interaction used between rigid plate and column surface top and bottom side. Figure 6 shows a typical finite element model adopted for modeling of concrete filled UVFC column. In the standard FEM feature model, the solid bottom plate that touches the base of the column is centered on all six points with the reference node. The solid plate over the top of the column is modeled as a language set in five directions, and movement is allowed on the column axis only in the reference area. The load is used as a removal of the vertical uniform plate on the upper plate near the center node of the solid plate. Confined concrete is subjected to triaxial compressive stresses; the effective stress and effective strain values may be represented by the uniaxial stress and strain values obtained from the stress-strain equation proposed by Saenz (1964). It is given as

$$f = \frac{E_{cc}\varepsilon}{1+(R+R_E-2)\left(\frac{\varepsilon}{\varepsilon_{cc}}\right)-(2R-1)\left(\frac{\varepsilon}{\varepsilon_{cc}}\right)^2+R\left(\frac{\varepsilon}{\varepsilon_{cc}}\right)^3}$$

where

$$R_E = \frac{E_{cc}\varepsilon_{cc}}{f_{cc}},\quad R = \frac{R_E(R_\sigma-1)}{(R_\varepsilon-1)^2}-\frac{1}{R_\varepsilon},\ R_\sigma\ \&\ R = 4$$

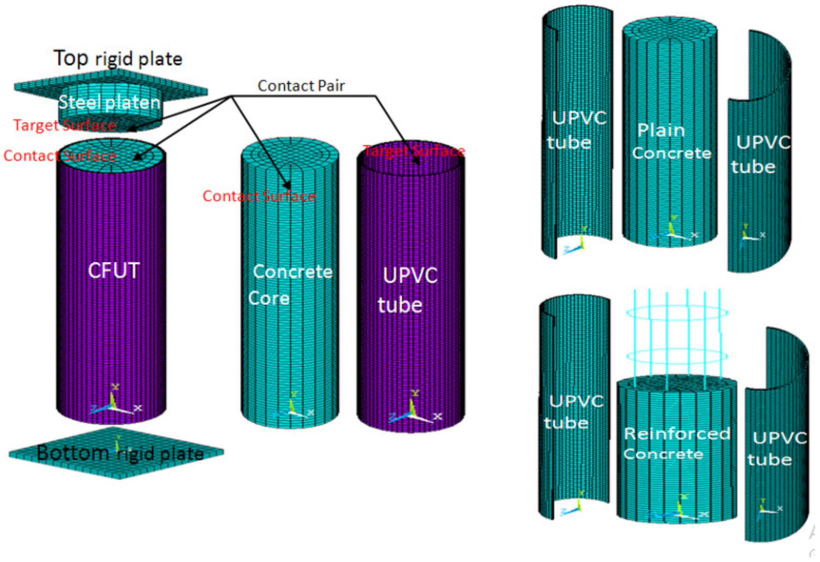

Figure 6. Finite Element modeling for concrete filled UPVC tube

4. Test Results and Discussion

In this study, further experiments were performed to determine the behavior of concrete enclosed in a UPVC tube. In this process the specimens are cast and tested using axial loading in the concrete context only. Internal hydrostatic pressure tests were performed to detect closed pressure. The confinement is the main governing factor to study the behavior of concrete filled tubes. In specimens where the jackets had lower degrees of radial strength compared to the concrete core, failure occurred mainly in the UPVC tubes and the concrete experienced relatively limited cracking in the form of shallow hairline cracks and other specimens where the influence of UPVC tube on strength of the column is more pronounced, the tube undergoes a variety of deformations such as local bulging, drumming, and buckling while it does not experience rupturing shown in Figure 7. The results of the test and numerical simulation of UPVC-filled concrete tubes are given in Table 4. Disable shape of a few tested samples and corresponding load-removable curves are planned.

The largest deviation of failure was observed between 10 mm and 14 mm. The angle of shear cracks from the horizontal axis is measured. It was between 63° and 65°. Post peak displacement is important with regard to the ductile behavior of objects. From the load-moving curve, it was found that the migration behind the maximum load was approximately 5 mm-10 mm. Load curves found in numerical analysis and accuracy checking. Typical variation of loading curves-removal of templates made of UPVC tubes with different width of the same class and the same width of different class respectively. It can be seen in Figure 7 that the initial slope of the curves increases as the diameter of the tubes increases and the slope of the post is almost the same.

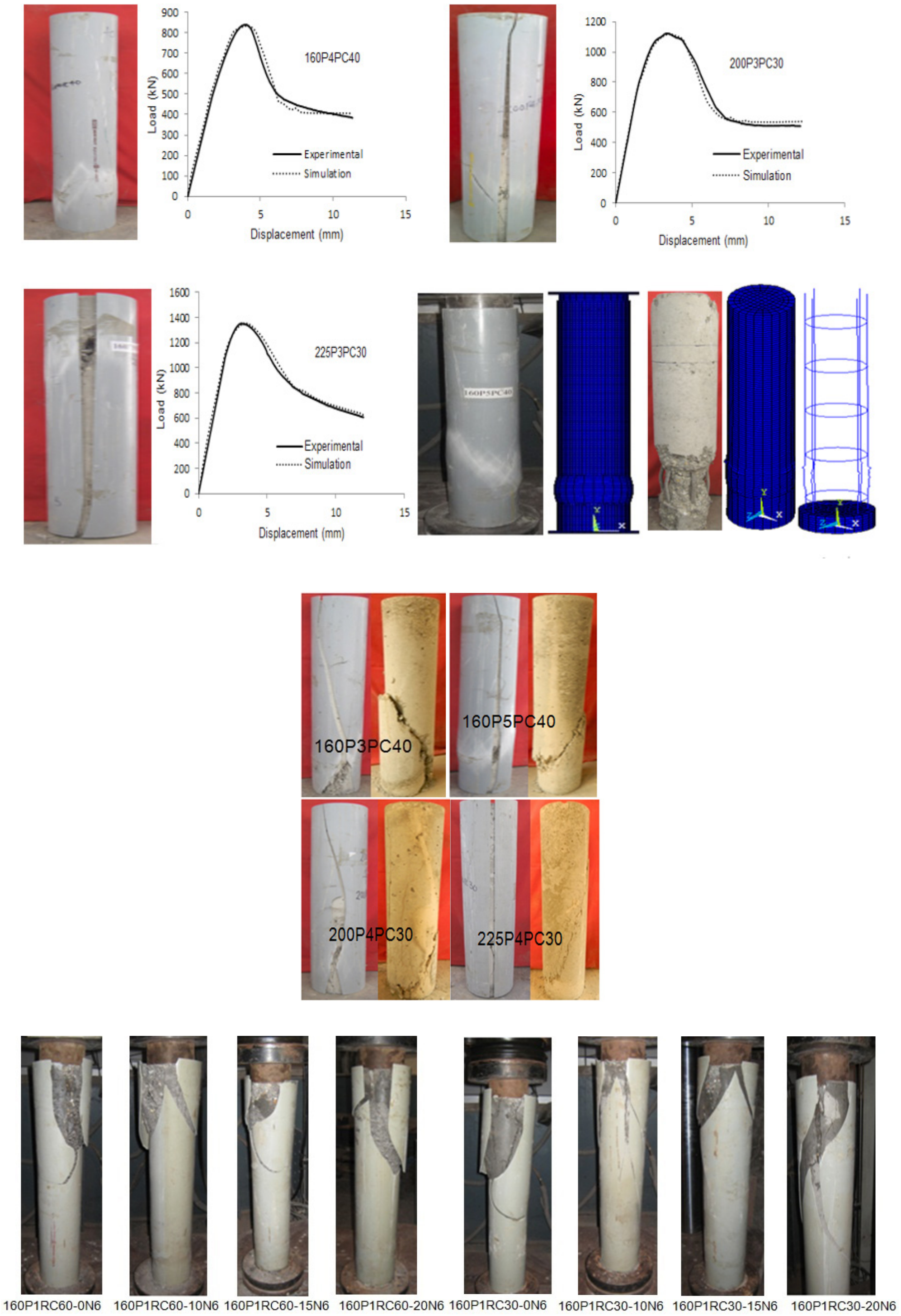

Figure 7. Experimental Results

Table 4. Experimental and fem Modeling results

Specimen	Ultimate Load (kN)		Constraining parameter $\alpha=A_p f_u/A_c f_c$	Confinement ratio $\beta=(f_l/f_c)$	Mode of failure	Failure load	Max. strain at failure
	Experimental	FEM Modeling					
160P3PC30	758	752	0.067	0.034	Shear cracks with slight bulge	348.28	0.0169
160P4PC30	769	763	0.089	0.045		350.70	0.0150
160P5PC30	793	789	0.123	0.062		372.08	0.0149
200P3PC30	1123	1128	0.081	0.041		509.40	0.0151
200P4PC30	1142	1135	0.114	0.057		656.69	0.0149
200P5PC30	1182	1177	0.125	0.063		614.16	0.0140
225P3PC30	1352	1354	0.107	0.053		607.22	0.0150
225P4PC30	1420	1412	0.119	0.059		695.44	0.0146
225P5PC30	1491	1482	0.125	0.062		772.05	0.0138
160P3PC40	816	812	0.060	0.030		324.59	0.0155
160P4PC40	839	832	0.080	0.040		383.80	0.0142
160P5PC40	850	844	0.111	0.055		456.14	0.0132
200P3PC40	1231	1222	0.073	0.036		564.15	0.0138
200P4PC40	1245	1239	0.102	0.051		598.87	0.0138
200P5PC40	1280	1276	0.113	0.056		650.86	0.0130
225P3PC40	1486	1472	0.096	0.048		693.89	0.0143
225P4PC40	1550	1539	0.107	0.054		759.42	0.0134
225P5PC40	1610	1598	0.112	0.056		806.35	0.0128

5. Concluding Remarks

In this study, a series of tests were performed on UPVC-confined columns. A new type of composite column, which can be obtained by filling a plastic container with non-plastic poly vinyl chloride (UPVC) is proposed and investigated. Based on the results obtained from the experiments and finite element analysis of UPVC-filled concrete tubes, the following conclusions can be derived.

- A stress-strain model enclosed by a UPVC tube is proposed. This model is achieved by changing the stress-strain model of concrete bound with different materials such as steel.
- For specimens made from lower concrete strength, the UPVC tube in a concrete filled UPVC tube column contributed significantly to the axial load carrying capability. The load-carrying capacity in a confined state for a column with an aspect ratio of two (h/D=2) was 1.12-1.65 times the sum of individual capacity in an unconfined state.
- The concrete was complete with shallow cracks and cracking occurred in the UPVC tube. On the other hand, when the tube was relatively strong, the concrete navel had deep and wide cracks while the tubes maintained their integrity without cracking and damage to the surface. Failure of all specimens leads by development of shear crack and macrocracks with slight bulging.
- This study used to propose a model to predict the ultimate strength of UPVC confined concrete columns.
- The strain at break for short specimens tested ranges from 1.25% to 1.70%. The 2t/D ratio and h/D ratio both had an effect on the post-peak stress-strain behaviour of UPVC confined concrete. As the 2t/D ratio increased, the absolute value of the slope decreased.
- The behavior of the load-compression curve depends on the ambient pressure of the pipe and the compressive strength of the concrete. The absolute value of the slope of the curve increases with increasing concrete strength and decreases with increasing ambient pressure.
- The UPVC confinement improved the columns' ductility and energy absorption.

Credit Authorship Contribution Statement

Manish Sharma: Investigation, Formal analysis, Re-sources, Writing - original draft. **Md. Imteyaz Ansari:** Overall guidance, Methodology and Supervision. **Nazrul Islam:** Conceptualization, Writing - review & editing, Visualization, Supervision.

Funding

The authors received no financial support for the research, authorship, and/or publication of this article.

Acknowledgments

The authors warmly acknowledge the computing facilities provided by the Head of the Civil Engineering Department, Faculty of Engineering and Technology, Jamia Millia Islamia, New Delhi-110025, India. For carrying out the present finite element simulations. Sincere thanks are also due to learned Reviewers for their critical review and suggestions to improve the manuscript in the present form.

Conflict of Interest

The authors declare that they have no known competing financial interests or personal relationships that could have appeared to influence the work reported in this paper.

References

[1] Yu, F., Xu, G., Niu, D., et al., 2018. Experimental study on PVC-CFRP confined concrete columns under low cyclic loading. Construction and Building Materials. 177, 287-302.

[2] Gao, C., Huang, L., Yan, L., et al., 2019. Strength and ductility improvement of recycled aggregate concrete by polyester FRP-PVC tube confinement. Composites. 162, 178-197.

[3] Wang, J.Y., Yang, Q.B., 2012. Investigation on compressive behaviors of thermoplastic pipe confined concrete. Construction and Building Materials. 35, 578-585.

[4] Huang, C.S., Yeh, Y.K., Liu, G.Y., et al., 2002. Axial load behavior of stiffened concrete filled steel columns. Journal of Structural Engineering. 128(9), 1222-1230.

[5] Wang, Z.B., Tao, Z., Han, L.H., et al., 2017. Strength, stiffness and ductility of concrete-filled steel columns under axial compression. Engineering Structures. 135, 209-221.

[6] Saadon, A.S., 2010. Experimental and Theoretical Investigation of PVC Concrete composite Columns. University of Basrah.

[7] Hsie, M., Tu, C., Song, P.S., 2008. Mechanical properties of polypropylene hybrid fiberreinforced concrete. Materials Science and Engineering: A. 494, 153-157.

[8] Sun, Z., Xu, Q., 2009. Microscopic, physical, and mechanical analysis of polypropylene fiber reinforced concrete. Materials Science & Engineering A. 527, 198-204.

[9] Gupta, P.K., Verma, V.K., 2016. Study of concrete-filled unplasticized poly-vinyl chloride tubes in marine environment. Proceedings of the Institution of Mechanical Engineers, Part M: Journal of Engineering for the Maritime Environment. 230, 229-240.

[10] Wang, J.Y., Yang, Q.B., 2010. Experimental study on mechanical properties of concrete confined with plastic pipes. Aci Materials Journal. 107(2), 132-137.

[11] Ragab, A.R., Mahmoud, M.A., Khorshied, S.A., 2001. Yielding of commercial poly (vinyl chloride) pipe material. Journal of Applied Polymer Science. 81, 991-999.

[12] Sun, Z., Xu, Q., 2009. Microscopic, physical, and mechanical analysis of polypropylene fiber reinforced concrete. Materials Science & Engineering A. 527, 198-204.

[13] Bangash, M.Y., 2001. Manual of numerical methods in concrete. London: Thomas Telford.

[14] ASTM-D638-10. Standard test method for tensile properties of plastics, ASTM International, United States.

[15] Gupta, P.K., Verma, V.K., 2021. Finite element modelling of load-carrying capacity of concrete-filled Unplasticised polyvinyl chloride (UPVC) tubes exposed to marine environment. Ships and Offshore Structures. 16(3), 271-279.

BILINGUAL PUBLISHING CO.
Pioneer of Global Academics Since 1984

Journal of Mechanical Materials and Mechanics Research
https://ojs.bilpublishing.com/index.php/jmmmr

EDITORIAL

Open Issues in Continuum Modelling of Carbon Nanotubes

Matteo Strozzi[*]

Department of Sciences and Methods for Engineering, University of Modena and Reggio Emilia, Reggio Emilia, 42122, Italy

ARTICLE INFO

Article history
Received: 1 May 2022
Accepted: 5 May 2022
Published Online: 8 May 2022

Carbon nanotubes (CNTs) were discovered in 1991 inside NEC Corporation laboratories by S. Iijima, who studied the synthesis of fullerenes and first prepared a new type of carbon structures, referred to as CNTs, which were described as "helical microtubules of graphitic carbon" [1].

Since CNTs have very high Young's modulus and tensile strength, together with very small diameter, then they can reach natural frequencies of the THz order and therefore can be used as high sensitivity resonators in many electro-mechanical devices such as sensors, charge detectors and oscillators.

In addition, the extremely high electric and thermal conductivity of CNTs, together with the very high transparency in the visible range, makes them promising candidates for innovative applications that include heat exchangers and energy conversion systems, with the role of advanced catalyst supports or electrodes in solar and fuel cells.

CNTs are divided in two main classes: single-walled carbon nanotubes (SWCNTs), given by graphene sheets rolled into cylinders, and multi-walled carbon nanotubes (MWCNTs), composed by concentric SWCNTs, where the different cylinders are connected by van der Waals interaction forces.

Due to their relevant applications in several mechanical components, vibrations of CNTs have been attracted much attention from researchers. Specifically, CNT vibrations have been studied by means of experimental, atomistic mechanics and continuum mechanics methods.

Resonant Raman spectroscopy (RRS) starts from the experimental measurement of CNT diameter by means of atomic force microscopy and investigates atomic structure, chirality and natural frequencies of CNTs. However, due to the high technological complexity and costs, experimental methods cannot be considered as efficient

---

*Corresponding Author:
Matteo Strozzi,
Department of Sciences and Methods for Engineering, University of Modena and Reggio Emilia, Reggio Emilia, 42122, Italy;
Email: matteo.strozzi@unimore.it

DOI: https://doi.org/10.30564/jmmmr.v5i1.4693

approaches to study mechanical behaviour of CNTs.

Molecular dynamics (MD) simulations consider CNT atoms as interacting point-like masses, where the vibrations of the free atoms are recorded for a certain time duration at fixed temperature. However, due to the high computational effort, atomistic mechanics methods cannot be easily applied to CNT structural simulation, specially MWCNTs, which incorporate a large number of carbon atoms.

Since theoretical models based on continuum mechanics are computationally more efficient than MD simulations and do not present the technological complexity and high costs of RRS, then continuous elastic models are the most commonly adopted methods for the study of CNT vibrations.

In these models, it is assumed that the effective discrete structure of CNTs can be replaced by means of an equivalent homogeneous elastic structure with a continuous distribution of mass and stiffness, not considering their intrinsic atomic nature and so reducing the number of degrees of freedom.

In order to carefully investigate the validity of continuum mechanics approaches for CNT vibrations, in the cases when the lattice structure of CNT is modelled with a continuous circular cylindrical shell, some very important open issues should be taken into account and properly discussed.

The first relevant issue to be taken into account in the modelling of CNTs as continuous elastic shells is given by anisotropy. CNTs are usually modelled as isotropic elastic shells; however, they present a chirality-induced anisotropic behaviour due to their discrete nature that cannot be captured by using an isotropic shell model.

To this aim, Chang et al. [2] developed a molecular mechanics model, called “stick-spiral model”, able to correctly predict chirality and size-dependent elastic properties of CNTs. They found explicit expressions for longitudinal Young’s modulus and Poisson’s ratio, circumferential Young’s modulus and Poisson’s ratio, and longitudinal shear modulus in case of chiral SWCNTs. This molecular based anisotropic elastic shell model including chirality effects was validated via comparisons with RRS and MD data, proving that the classical relationship of isotropic elastic continuum mechanics between Young’s and shear modulus is not valid for SWCNTs.

In addition to anisotropy, another relevant issue in the modelling of CNTs as continuous elastic shells is given by nonlocality. Classical continuum mechanics models assume that the stress state at a given point of the body is uniquely dependent on the strain state at that point, and they do not admit any intrinsic size dependence in the elastic constitutive equations; therefore, they are not able to identify the small-scale effect on CNT mechanical behaviour. On the other hand, Eringen’s nonlocal elasticity theory assumes that the stress state at a given point of a body is a function of the strain field at every point of the body, where the scale effect is inserted in the constitutive equations as a constant nonlocal parameter.

Starting from Eringen’s nonlocal elasticity theory, Fazelzadeh and Ghavanloo [3] developed a refined nonlocal anisotropic elastic shell model by calibrating the value of nonlocal parameter with the results of MD simulations to obtain the linear vibrations of CNTs with different chiralities, geometries and boundary conditions.

Besides anisotropy and nonlocality, in the specific case of MWCNTs a third relevant issue to be taken into consideration in the continuum modelling is given by van der Waals interactions between the concentric SWCNTs.

Ru [4] proposed a linear relationship between pressure due to van der Waals interaction and radial displacement for the buckling and vibration analysis of MWCNTs in which the interaction coefficient is constant, i.e., it is not dependent on the radius of the individual SWCNT. However, it is clear that this simplified formulation is not accurate in modelling van der Waals interactions.

In order to accurately describe van der Waals interaction forces in MWCNTs, He et al. [5] proposed a linear relationship between pressure due to van der Waals interaction and radial displacement where the interaction coefficient is radius-dependent. By using this refined formulation, natural frequencies of MWCNTs were analysed for different geometries and chiralities, obtaining an excellent agreement with MD results.

To conclude, as reported above, several advanced models have been proposed in the last decades for the continuum modelling of carbon nanotubes. However, it is important to develop new more accurate models, able to better capture the actual CNT behaviour derived by experiments and MD simulations. To this purpose, *Journal of Mechanical Materials and Mechanics Research*, a peer-review and open access journal, provides a good service platform for researchers to publish their works on advances in continuum modelling of carbon nanotubes.

Conflict of Interest

There is no conflict of interest.

References

[1] Iijima, S., 1991. Helical microtubules of graphitic carbon. Nature. 354, 56-58.

[2] Chang, T., Geng, J., Guo, X., 2006. Prediction of chi-

rality- and size-dependent elastic properties of single walled carbon nanotubes via a molecular mechanics model. Proceedings of the Royal Society A. 462, 2523-2540.

[3] Fazelzadeh, S.A., Ghavanloo, E., 2012. Nonlocal anisotropic elastic shell model for vibrations of single-walled carbon nanotubes with arbitrary chirality. Composite Structures. 94, 1016-1022.

[4] Ru, C.Q., 2001. Axially compressed buckling of a double-walled carbon nanotube embedded in an elastic medium. Journal of the Mechanics and Physics of Solids. 49, 1265-1279.

[5] He, X.Q., Eisenberger, M., Liew, K., 2006. The effect of van der Waals interaction modelling on the vibration characteristics of multi-walled carbon nanotubes. Journal of Applied Physics. 100, 124-317.

Journal of Mechanical Materials and Mechanics Research
https://ojs.bilpublishing.com/index.php/jmmmr

ARTICLE

Adverse Effects of Condenser Cooling Seawater Temperature, Fouling, and Salinity on the Output Power and Thermal Efficiency of BWR NNPs

Said M. A. Ibrahim* Ismail M. A. Aggour
Mechanical Engineering Department, Faculty of Engineering, Al-Azhar University, Cairo, Egypt

ARTICLE INFO

Article history
Received: 10 April 2022
Accepted: 6 May 2022
Published Online: 13 May 2022

Keywords:
BWR NPP
Thermal efficiency
Temperature
Fouling
Salinity

ABSTRACT

Increasing the thermal efficiency in newly designed power stations is a priority. Keeping the efficiency in existed plants close to the rated one is of paramount importance. This research contributes to investigating the adverse effects of changes in condenser seawater coolant characteristics, (temperature, fouling, and salinity), on the thermal performance of a Boiling Water Reactor Nuclear Power Plant (BWR) NPP. A mathematical model is developed to relate seawater cooling temperature, fouling, and salinity to output power and thermal efficiency. The model also explains the impact of the condenser performance on power and efficiency. The thermal efficiency of the considered BWR NPP is reduced by 2.26% for a combined extreme increases in the condenser cooling seawater temperature, fouling factor of seawater and treated boiler feed water, and salinity by 10 °C, 0.0002, 0.00001 m^2K/W, and 100 g/kg, respectively. A rise in the condenser efficiency from 40% - 100% results in an increase in the output power by 7.049%, and the thermal efficiency increases by about 2.62%. Conclusions are useful for reactor's design.

1. Introduction

The ultimate goal of designers of power stations whether thermal or nuclear, from the thermodynamic point of view, is to attain the maximum possible thermal efficiency. For operators thereafter, the job is to maintain and run the station close to the rated efficiency. The low temperature sink is the heat rejected by the condenser, which is a crucial component of power stations. Its proper operation according to the design data is of paramount importance for the station to operate efficiently. There is a desirability of having a high temperature internally and a low temperature in the external environment. This consideration gives rise to desirably siting power plants alongside cold water. Most power plants have higher efficiencies in winter than in summer.

A power plant is designed according to pre-determined design conditions for optimum efficiency. However, in

---

*Corresponding Author:
Said M. A. Ibrahim,
Mechanical Engineering Department, Faculty of Engineering, Al-Azhar University, Cairo, Egypt;
Email: prof.dr.said@hotmail.com

DOI: https://doi.org/10.30564/jmmmr.v5i1.4617

practice rated conditions cannot be maintained as the time goes by, because inlet conditions are not as per design data, hence the efficiency and output power drop. A steam plant and the second cycle of a nuclear plant are composed of many components; each is designed for optimum operation in order to satisfy the overall plant efficiency. The condenser is not the largest piece of equipment in the plant, but it is a key item in determining the plant efficiency.

Surface condensers are the types usually used in power plants. The condenser is necessarily a large piece of equipment because more than 60% of the thermal energy produced by a plant ends up as low enthalpy heat because of the thermodynamic limitation of the Rankine cycle. This reject heat is dissipated by the condenser to the environment. The heat transfer area in a power plant's surface condenser easily dwarfs any other heat exchanger in the plant. The lower heat sink temperature means higher Carnot cycle efficiency. The upper heat reservoir is limited by material considerations. Therefore, attaining the lowest possible condensing temperature in the heat sink of the Rankine cycle is a primary goal in surface condenser design. Since the saturation temperature and pressure of steam are proportionally related at low pressures, the objective of low condensing temperature necessitates a low condenser operating pressure. The condenser reduces the turbine exhaust pressure so as to increase the specific turbine output.

The steam power plant performance strongly depends on its low pressure end operating conditions, where the condenser is the key component to do this. The thermal efficiency of power plants mainly depends on its turbine-condenser performance. Generally, as the condenser pressure increases, due to changes in its cooling water characteristics, both thermal efficiency and net output power decrease and the steam consumption increases.

Condensers in power plants are usually cooled by water. Thus, factors affecting the condenser performance are related to characteristics of the condenser cooling water. The present research deals with nuclear power plants (NPPs), which are mostly located near seas, and condensers are cooled by seawater. Three properties of the condenser cooling seawater are important: temperature, fouling, and salinity. The adverse effects of these factors, due to deviations from design values, on the thermal performance of a BWR NPP are investigated. In fossil fuel power plants (PPs), some of the heat discharged is in the flue gases through the stack, whereas in a NPP virtually all the waste heat has to be dumped into the condenser cooling water. Thermal PPs have an intrinsic advantage which enables them to run their internal boilers at higher temperatures than those with finely engineered nuclear fuel assemblies which must avoid damage for safety. This means that the efficiency of modern fossil fuelled plants is typically higher than that of nuclear plants. A nuclear or thermal plant running at 33% thermal efficiency, for instance will need to dump more heat than ones with 36% efficiency. Nuclear plants currently being built have about 34%-36% thermal efficiency, depending on the site (especially concerning water temperature). Older NPPs are often only 32%-33% efficient.

The water temperature in oceans, lakes, seas, and rivers differs significantly from one site to another. The seasonal variations of water temperature differ depending on the location. The design of the condenser in a power station depends on the inlet cooling water temperature. Therefore, the station should be sited carefully, according to the cooling water temperature of the source; low temperature sites with less seasonal variations are preferable if in hand. Sometimes it is unavoidable to locate the plant on a high temperature water source like in the Arabian Gulf region. As the temperature of the condenser cooling water changes, the condenser pressure is directly affected, and this reflects on the plant performance. Cooling water temperature increase means condenser pressure increase, and consequently plant efficiency decrease. It has been concluded that for a proposed PWR NPP, the output power and the thermal efficiency of the plant decrease by approximately 0.3929% and 0.16%, respectively, for 1 °C increase in the temperature of the condenser cooling seawater [1]. It is shown that an increase in the inlet cooling seawater temperature of 15 °C reduces the efficiency and the output power by 2% and 6%, respectively, of the 1450 MW power cycle of the APR 1400 PWR NPP in the United Arab Emirates located on the Arabian Gulf [2]. A study on the effect of cooling water temperature on the thermal efficiency of a PWR NPP, found that an increase of 1 °C of the coolant water results in a decrease of about 0.45% and 0.12% in the power output and thermal efficiency of the plant, respectively [3]. For nuclear power plants, a rise in temperature of 1 °C reduces the nuclear power by about 0.5% through its effect on the thermal efficiency [4]. For a 225 MW steam PP, every 1 °C increase in the condenser cooling seawater temperature, the output power of the plant decreased by about 0.171%, the condenser pressure increased by about 5.146%, and the plant efficiency decreased by approximately 0.168% [5]. Reference [6] investigated, by a thermodynamic model, the impact of flow rate, temperature and velocity of the cooling water on the heat transfer and condenser effectiveness, for a coal fired plant, and found that 1 °C increase in the inlet temperature of cooling water leads to deviation of the condenser pressure by 0.59 kPa, which reduces the cycle heat transfer rate by 0.36% and the unit generation by 33 MW. An experimental work on the performance of a steam condenser in a 600 MW thermal PP depicted that the plant efficiency increased from 38.83% to 39.45% by reducing the condenser pressure to 65.21 bar [7]. A research on the effect of the condenser [8]. For an increase of 30 °C in the inlet cooling water temperature, the annual cash flow decreases by million 3.6 Dollars, and the electricity production cost is increased to 0.148 cent/kWh [8]. A Rankine cycle model for the secondary cycle of a VVER 1200 NPP showed a decrease in the thermal efficiency from 37.44% to 33.65% due to an increase in the condenser pressure from 4 kPa - 15 kPa, which was attributed to increase in the condenser cooling temperature and atmospheric temperature [9].

Fouling of heat exchangers may be defined as the accumulation of undesirable deposits on heat transfer surfaces. The fouled layer creates an additional resistance to heat transfer, and the contraction of the flow area, due to fouling, results in an increased flow velocity for a given volumetric flow rate. Furthermore, the deposit is usually hydro dynamically rough so that there is an increased resistance to the fluid flow across the deposited surface. In shell and tube steam condensers, the cooling water flow velocity is usually low, and this gives rise to more fouling accumulation in the tubes. Thus, the problems associated with condenser fouling will be more pronounced. Therefore, the consequences of fouling are, in general, a reduction in the exchanger efficiency and other associated operating problems including excessive pressure drop across the exchanger. This affects the plant thermal performance. In order to cope with the expected fouling, the heat exchanger should have an additional area over that required to give the same heat rate in the clean condition. A model for studying the effect of changes in the condenser cooling seawater fouling on the thermal efficiency and output power of a PWR NPP, indicated that an increase in the condenser cooling seawater fouling factor in the range 0.00015 m^2K/W-0.00035 m^2K/W had led to a decrease in the plant output power and thermal efficiency of 1.36% and 0.448%, respectively [10]. The effect of the thermal resistance of fouling on the power output of a condensing turbine, after one year of operation, indicated that for old condensers the fouling resistance could reach 0.0007 m^2K/W, and this reduced the turbine power output by up to 4.1%, whereas for new condensers, the power output drop did not exceed 1.5% [11]. A model to predict the effect of fouling effect of fouling on the thermal performance of evaporative coolers and condensers showed that the maximum decrease in effectiveness due to fouling was 78% for condensers [12]. Research published [13] showed that undesirable design procedures and operation problems of heat exchangers typically oversize them by 70%-80% of which 30%-50% is attributed to fouling. It has been stated that if the overall heat transfer coefficient for the fouled condition is ½ the coefficient for clean condition, then the heat transfer area is doubled, and that the choice of the fouling resistance is crucial not only for efficient operation of the heat exchanger and its operating cost, but also on its capital cost [14]. A study on the impact of water fouling properties on the thermal and hydraulic parameters of the shell and tube heat exchanger tubes demonstrated that minor change in the fouling layer thickness has direct effect on the heat transfer compared to the pressure drop for the heat exchanger [15]. A model has been provided to study the effect of fouling on the effectiveness and water outlet temperatures of cooling towers demonstrated about 0.6% decrease in effectiveness and about 1.2% increase in the water outlet temperature [16]. Reference [17] studied the bio fouling control of seawater to achieve efficient operation of a power station, and reported that it is important for power plant designers to choose the most suitable control method to combat bio fouling in practical, economical, and environmentally acceptable manners.

Salinity is the saltiness or the quantity of salt dissolved in water, which is called saline water. This is usually measured in g salt/kg seawater. Salinity is a thermodynamic state variable that, along with temperature and pressure, governs physical characteristics like the density and heat capacity of saline water. Thus, changes in the salinity of the condenser cooling seawater could affect its performance. Salinity in closed seas, like the Dead Sea is much higher than that in oceans and large area seas, rivers and lakes have very lower salinities in comparison. A model was provided to obtain the effect of salinity of the condenser cooling seawater of a PWR NPP on the thermo-physical properties of seawater on the thermal performance of the plant revealed that increasing the condenser cooling seawater salinity by 10 g/kg, 50 g/kg, and 100 g/kg resulted in losses in the thermal efficiency of the plant by 0.011%, 0.06%, and 0.14%, respectively with respective reductions in the output power for the same salinity values of 0.033%, 0.039%, and 0.044% [18]. An investigation on the effect of changing the salt content on many properties of seawater, such as density, thermal expansion, temperature of maximum density, viscosity, speed of sound, vapor pressure, etc. gives that knowledge of the way these parameters change, as well as the processes that cause the changes, are essential for the design of systems that will effectively operate in the ocean [19]. A model relating the condenser cooling seawater salinity and temperature and the thermal efficiency of a PWR NPP reported a loss of 0.2% in the efficiency, for temperature and salinity values of 5 K, and 10000 ppm [20]. Reference [21] investigated the thermal performance of a seawater cooling tower experimentally and theoretically, and found that the air effectiveness decreased with increasing the seawater salinity, with a maximum decrease of 15% for a salinity of 85 g/kg. A work connected with injecting seawater into the nuclear reactors of the Fukushima disaster (Japan, 2011), in order to cool down fuel elements, illustrated that seawater affects the heat transfer due to changes in salinity and other physical properties of the coolant [22].

We could not detect research work concerning the combined effect of temperature, fouling, and salinity of the condenser cooling seawater on the thermal performance of NPPs except that by Ibrahim et al. [23]. This study focused on a proposed PWR NPP, and showed that a significant loss in the plant output power and thermal efficiency of up to 8.242% and 2.77%, respectively, can result from an increase in the condenser cooling seawater temperature from 15 °C-30 °C, fouling factor from 0.00015 m^2K/W-0.00035 m^2K/W, and salinity from 0 g/kg.-100 g/kg.

Since the efficiency of NPPs is lower than that of thermal PPs, therefore, it is important to mitigate or prevent if at all possible all factors that reduce their efficiency. To achieve this, relations between such factors and the thermal efficiency and output power of NPPs should be studied and analyzed. The current research contributes to the adverse effects of variations in the condenser inlet cooling seawater temperature, fouling, and salinity on the thermal efficiency and power output of a proposed BWR NPP. The paper includes the individual effects of these properties as well their combined impacts. We developed a model, based on thermodynamic and heat balance considerations, to calculate the required effects, and numerical solutions were performed by a computer program. The work is related to a BWR NPP, since there is no research conducted on this type of plant relevant to the subject of the current research.

2. The Selected BWR NPP

The present study is concerned with the complete cycle of a typical BWR NPP. An OKG's Oskarshamn 3 (O3) NPP is selected as a case study of such a plant. Oskarshamn is one of three active nuclear power plants in Sweden. The plant is located about 30 kilometers north of Oskarshamn, on the Baltic Sea coast. In 1985, Oskarshamn 3 was phased in online and reached its full power of 1050 MW. In 1989, the power of O3 was scaled up to a maximum of 1200 MW. In 2012, the power was further increased to 1450 MW, making O3 one of the largest BWRs in the world.

The plant consists typically of a BWR, reactor coolant pump, high-pressure steam turbine (HPST), three low pressure steam turbines (LPST), moisture separator and reheater (MS/R), deaerator feed water heater, two high-pressure feed water heaters (HPFWH), and three low pressure feed water heaters (LPFWH), condenser, bypass valve (BPV) which is essential to keep the pressure inside the reactor at 70 bar to ensure good and stable moderation, and necessary pumps (feed water and condensate pumps). Figure 1 is a schematic diagram showing the main components of the proposed plant [24].

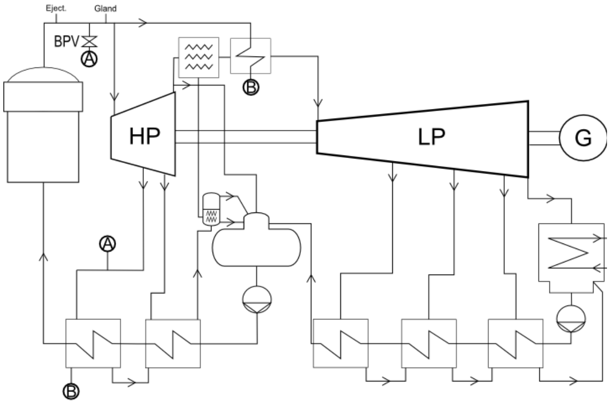

Figure 1. A Schematic of main components of the proposed BWR NPP

Technical design data of the Oskarshamn 3 NPP are given in Table 1.

Table 1. Design data of the Oskarshamn 3 BWR NPP

Vapor data		
before high pressure turbine	MPa / °C	6.5 / 283
after high pressure turbine	MPa / °C	0.97 / 179
in condenser	kPa / °C	4.0 / 30
Number of preheating steps		6
- low pressure preheating	stages	4
- high pressure preheating		2
Feed water temperature	°C	218
Generator power	MW	1450
Gross efficiency	%	36.5
Aggregate net power	MW	1400
Steam flow rate	Kg / s	2115
Condenser cooling water flow rate	m^3 / s	55
Condenser cooling water inlet temperature	°C	5
Condenser cooling water temperature increase	°C	10.5

3. The Present Theoretical Model

3.1 Model Calculation Data

The present calculations were made for these values:

- The range of change of cooling water temperature is 5 °C-15 °C.
- The range of change of the fouling factor, F is

0.00015 m^2K/W-0.00035 m^2K/W.

- The treated boiler feed water range is 0.00005 m^2K/W-0.00015 m^2K/W.
- The change of cooling seawater salinity S_p is 0 g/kg-100 g/kg.

The combined effect of cooling seawater temperature, fouling factor, and salinity was calculated for the above given values.

3.2 Model Assumptions

(1) Thermodynamic conditions of the steam at exit of the nuclear reactor are fixed.

(2) Thermal power of the BWR changes slowly to provide constant thermodynamic properties of the steam at exit from the nuclear reactor, since the variation in the cooling water temperature occurs seasonally and very slowly.

(3) Constant cooling water temperature difference.

(4) The condenser vacuum pressure varies with the temperature of cooling water extracted from the sea at fixed mass flow rate into the condenser.

(5) Constant mass flow rates of condensate and cooling water.

(6) Fixed total surface area of condenser tubes and material properties.

(7) There is no pressure drop across the condenser.

(8) Constant condenser heat transfer area and heat load.

(9) Potential and kinetic energies of the flow and heat losses from all equipment and pipes are negligible.

3.3 Model Formulation and Equations

3.3.1 Thermodynamic Analysis

The energy balance equations for the various processes involving steady flow equipment such as the nuclear reactor, turbine, pumps, and condenser are:

♦ Heat added to steam from reactor, Q_{add} is

$$Q_{add} = \dot{m}_{st}\,(h_{out} - h_{in})\ \text{kW} \qquad (1)$$

where $\dot{m}_{st}$= mass flow rate of steam exit from reactor or steam generator, kg/s, h_{in} = enthalpy of feed water inlet to reactor or steam generator, kJ/kg, and h_{out} = enthalpy of steam outlet from reactor or steam generator, kJ/kg.

♦ Total turbine work, W_T is

$$W_T = W_{HPT} + W_{LPT}\ \text{kW} \qquad (2)$$

$$W_{HPT} = \dot{m}_{st}\,(h_{in} - h_{out})\ \text{kW} \qquad (3)$$

$$W_{LPT} = \dot{m}_{st}\,(h_{in} - h_{out})\ \text{kW} \qquad (4)$$

where $\dot{m}_{st}$ = mass flow rate of steam inlet to turbine, kg/s, h_{in} = enthalpy of steam inlet to turbine, kJ/kg, h_{out} = enthalpy of steam outlet from turbine, kJ/kg, W_{HPT}= high pressure turbine work, kW, and W_{LPT} = low pressure turbine work, kW.

♦ Pump work, W_P is

$$W_p = W_{cp} + W_{fwp}\ \text{kW} \qquad (5)$$

$$W_{fwp} = \dot{m}_{fw}\,(h_{in} - h_{out})\ \text{kW} \qquad (6)$$

$$W_{cp} = \dot{m}_{fw}\,(h_{in} - h_{out})\ \text{kW} \qquad (7)$$

where $\dot{m}_{fw}$ = mass flow rate of feed water inlet to pump, kg/s, h_{in} = enthalpy of feed water to pump, kJ/kg, h_{out} = enthalpy of feed water outlet from pump, kJ/kg, W_{fwp} = feed water pump work, kW, and W_{cp} = condensate pump work, kW.

♦ Heat rejected from condenser, Q_{Rej} is

$$Q_{Rej} = (\dot{m}_{mix} * h_{in} - \dot{m}_{fw} * h_{out})\ \text{kW} \qquad (8)$$

where $\dot{m}_{mix}$ = mass flow rate of mixture inlet to condenser, kg/s, h_{in} = enthalpy of mixture inlet to condenser, kJ/kg, and h_{out} = enthalpy of feed water outlet from condenser, kJ/kg.

♦ Net work done, W_{net} is

$$W_{net} = W_T - W_p\ \text{kW} \qquad (9)$$

♦ Cycle **efficiency, η_{th}** is

$$\eta_{th} = \frac{W_{net}}{Q_{add}}\ \% \qquad (10)$$

3.3.2 Heat Balance Equations

Heat Balance of Feed Water Heaters

A lower temperature than that of natural environment cannot be utilized, therefore, the large amount of heat rejected from the condenser is wasted. To mitigate such heat waste, regenerative feed water heaters (FWHs) are employed in which feed water is heated to its final temperature by extracted steam from various stages of turbines.

There are two different types of FWHs commonly used in power plants: open FWH, and closed FWHs, where a heat exchanger is used to transfer heat between two streams, which can be maintained at different pressures.

♦ Closed feed water heaters

Most feed water heaters are shell-and-tube heat exchangers, although some are of the header type. A few employ straight tubes, although the majority uses U-tubes, which are relatively tolerant to the thermal expansion during operation.

In shell and tube closed FWHs, the condensed steam, on the shell side, from each feed water heater drains successively to the next lower pressure heater and is returned to the feed water by means of heater drain pumps or through the condenser. The heat balance equation is

$$\dot{m}_{st} * (h_1 - h_2) = \dot{m}_{fw} * (h_{out} - h_{in}) \qquad (11)$$

where $\dot{m}_{st}$ = steam mass flow rate extracted from turbine to feed water heater, kg/s, $\dot{m}_{fw}$ = feed water mass flow rate inlet to feed water heater, kg/s, h_1 = enthalpy of steam inlet to feed water heater, kJ/kg, h_2 = enthalpy of steam outlet from feed water heater, kJ/kg, h_{in} = enthalpy of mixture inlet to feed water heater, kJ/kg, and h_{out}= enthalpy of feed water outlet from feed water heater, kJ/kg.

♦ Deaerator

Dissolved oxygen and carbon dioxide in the feed water fed to the boiler cause internal corrosion of pipes. Thus, it is extremely important to get rid of all dissolved gases from feed water, and this is achieved by using a deaerator, which is an open feed water heater. Equipment life can be extended at little or no cost by limiting the oxygen concentration to 5 ppb. Dissolved CO_2 is essentially completely removed by the deaerator.

Deaerators in steam generating systems of most thermal power plants use low pressure steam obtained from an extraction point in their steam turbine system. The heat balance is

$$(\dot{m}_{st} + \dot{m}_{fw}) * h_{out} = (\dot{m}_{st} * h_1) + (\dot{m}_{fw} * h_{in}) \tag{12}$$

where $\dot{m}_{st}$ = mass flow rate of Steam extracted from turbine to deaerator, kg/s, $\dot{m}_{fw}$ = mass flow rate of Feed water inlet to deaerator, kg/s, h_1 = enthalpy of steam inlet to deaerator, kJ/kg, h_{in} = enthalpy of feed water inlet to deaerator, kJ/kg, and h_{out} = enthalpy of feed water outlet from deaerator, kJ/kg.

Heat Balance of Moisture Separator and Reheater

During expansion through the HP section, the moisture content in the steam increases to approximately 12% at the HP turbine exhaust. Moisture in the steam reduces the mechanical efficiency in the LP turbines and causes erosion of LP turbine blades.

The separator may be separate from the reheater or integral with it. Separate separators usually employ centrifugal principles.. In integral ones, sudden changes in the steam direction, by means of vanes or baffles, causing lose in the moisture momentum, thus falls down and get separated from the steam. The heat balance of the separator is

$$\dot{m}_r * (h_1 - h_2) = (\dot{m}_s * h_s) + ((\dot{m}_{st} - \dot{m}_s) * h_{out}) - (\dot{m}_{st} * h_{in}) \tag{13}$$

where $\dot{m}_{st}$ = mass flow rate of steam inlet to moisture separator and reheater, kg/s, $\dot{m}_s$ = mass flow rate of water drained from moisture separator and reheater to deaerator, kg/s, $\dot{m}_r$ = mass flow rate of reheating steam inlet to moisture separator and reheater, kg/s, h_{in} = enthalpy of steam with moisture inlet to moisture separator and reheater, kJ/kg, h_{out} = enthalpy of superheated steam outlet from moisture separator and reheater, kJ/kg, h_s = enthalpy of water drained from moisture separator and reheater to deaerator, kJ/kg, h_1 = enthalpy of reheating steam inlet to moisture separator and reheater, kJ/kg, and h_2 = enthalpy of reheating steam outlet from moisture separator and reheater to steam generator, or feed water heater, kJ/kg.

Heat Balance of Cooling Water System (condenser)

The rise in cooling water temperature and mass flow rate is related to the heat rejected in the condenser as

$$Q_{Rej} = (\dot{m}_{mix} * h_{in}) - (\dot{m}_{fw} * h_{out}) \tag{14}$$

$$Q_{Rej} = \dot{m}_{CW} * C * \Delta T \tag{15}$$

$$\Delta T = (T_{cwo} - T_{cwi}) \tag{16}$$

$$Q_{Rej} = U * A * LMTD \tag{17}$$

$$LMTD = \left(\frac{(Tcwo - Tcwi)}{\ln\left(\frac{(Tc - Tcwi)}{(Tc - Tcwo)} \right)} \right) \tag{18}$$

where $\dot{m}_{CW}$= cooling water mass flow rate of condenser, kg/s, $\dot{m}_{fw}$= feed water mass flow rate of outlet from condenser, kg/ s, $\dot{m}_{mix}$= mixture mass flow rate inlet to condenser, kg/s, h_{in} = enthalpy of mixture inlet to condenser, kJ/kg, h_{out} = enthalpy of feed water outlet from condenser, kJ/kg, T_c = Condenser saturation temperature, °C, T_{cwo} = temperature of cooling water outlet from condenser, °C, T_{cwi} = temperature of cooling water inlet to condenser, °C, ΔT= temperature different between the cooling water exit and inlet temperature, °C, U = Overall heat transfer coefficient, W/m^2K, C = specific heat of water, kJ/kgK, A = heat transfer area, m^2, and LMTD = log mean temperature difference, °C.

3.4 Important Factors Affected by Changes in Cooling Seawater Temperature, Fouling Factor, and Salinity

♦ Inside overall heat transfer coefficient, U_i is

$$U_i = \frac{1}{(A_i * (R_i + R_w + R_o + R_{f,i} + R_{f,o}))} \ W/m^2K \tag{19}$$

where A_i = inside tube surface area, m^2, R_i = thermal resistance of inner seawater, K/W, R_o= thermal resistance of outer condensation film, K/W, R_w= thermal resistance of tube wall, K/W, $R_{f,i}$ = fouling factor thermal resistance inside condenser tubes, K/W, and $R_{f,o}$= fouling factor thermal resistance outside condenser tubes, K/W.

♦ Outside overall heat transfer coefficient, U_o is

$$U_o = \frac{1}{(A_o * (R_i + R_w + R_o + R_{f,i} + R_{f,o}))} \ W/m^2K \tag{20}$$

where A_o= outside tube surface area, m^2, R_i= thermal resistance of inner seawater, K/W, R_o =thermal resistance of outer condensation film, K/W, and R_w =thermal resistance of tube wall, K/W, $R_{f,i}$ = fouling factor thermal resistance inside condenser tubes, K/W, and $R_{f,o}$ = fouling factor thermal resistance outside condenser tubes, K/W.

♦ Thermal resistance of inner seawater, R_i is

$$R_i = \frac{1}{A_i * h_i} \text{ K/W} \quad (21)$$

where A_i= inside tube surface area, m^2, and h_i=heat transfer coefficient for flow inside circular tubes, W/m^2 K.

♦ Thermal resistance of outer seawater, R_o is

$$R_o = \frac{1}{A_o * h_o} \text{ K/W} \quad (22)$$

where A_o= outside tube surface area, m^2, and h_o= film condensation heat transfer coefficient in bundles of horizontal tubes, W/m^2K.

♦ Thermal resistance of tube wall, R_w is

$$R_w = \frac{\ln\left(\frac{r_o}{r_i}\right)}{2 \pi L k} \text{ K/W} \quad (23)$$

where k= thermal conductivity of tube, W/m K, r_o= outer radius, m, r_i= inner radius, m, and L= tube length, m.

♦ Thermal resistance of seawater fouling factor, R_f is

$$R_f = \frac{F}{A} \text{ K/W} \quad (24)$$

where A= tube surface area, m^2, and F= fouling factor, m^2 K/W.

♦ Heat transfer coefficient of flow inside circular tubes, h_i

$$h_i = \frac{N_u * k_{sw}}{d} \text{ W/m}^2\text{K} \quad (25)$$

where:

$$N_u = 0.023 * R_e^{0.8} * P_r^{0.4} \quad (26)$$

$$R_e = \frac{\rho_{sw} * V * d}{\mu_{sw}} \quad (27)$$

$$P_r = \frac{\mu_{sw} * C_{P,sw}}{k_{sw}} \quad (28)$$

where ρ_{sw}= seawater density, kg/m^3, V= flow velocity, m/s, d= tube diameter, m, μ_{sw}= seawater dynamic viscosity, N/m^2 s, k_{sw}= seawater thermal conductivity, W/m K, and $C_{p,sw}$= seawater specific heat capacity, J/kg K.

♦ Film condensation heat transfer coefficient in bundles of horizontal tubes, h_o is [25]

$$h_o = 0.725 \left(\frac{g * \rho_l * (\rho_l - \rho_V) * h_{fg} * k^3}{\mu_l * (T_{st} - T_W) * N_h * d_o}\right)^{0.25} \text{ W/m}^2\text{K} \quad (29)$$

where ρ_l= liquid density, kg/m^3, ρ_V= Steam or vapor density, kg/m^3, μ_l= liquid dynamic viscosity, $N/m^2.s$, T_{st}= steam or vapor saturation temperature, °C. N_h= number of horizontal tubes, h_{fg}= latent heat for condensation, kJ/kg, k= thermal conductivity of liquid, W/m K, g = acceleration of gravity, m/s^2, and T_w= condenser tube surface wall temperature, °C.

♦ Seawater density, ρ_{sw}

The density of seawater, ρ_{sw} as a function of temperature, pressure, and salinity is a fundamental oceanographic property. The thermo-physical seawater density correlation is given as [26]

$$\rho_{sw} = \left(\begin{matrix} (a_1 + a_2T + a_3T^2 + a_4T^3 + a_5T^4) + \\ (b_1S_p + b_2S_pT + b_3S_pT^2 + b_4S_pT^3 + b_5S_pT^4) \end{matrix}\right) \text{kg /m}^3 \quad (30)$$

where:

a_1=9.999×10^2, a_2= 2.034×10^{-2}, a_3=−6.162×10^{-3}, a_4=2.261×10^{-5}, a_5=−4.657×10^{-8},
b_1= 8.020×10^2, b_2= −2.001, b_3=1.677×10^{-2}, b_4=−3.060 ×10^{-5}, b_5=−1.613×10^{-5}, and valid for ρ_{sw} in (kg/m^3) for $0 \leq T \leq 180$ °C, and $0 \leq S_p \leq 0.16$ kg/kg, with accuracy ± 0.1 %.

♦ Seawater specific heat, C_{psw}

The specific heat of seawater, C_{psw} changes as a function of both temperature and salinity. The thermo-physical seawater specific heat correlation is [26]

$$C_{psw} = A + B\,T + C\,T^2 + D\,T^3 \text{ kJ/kg K} \quad (31)$$

where:

$A = 5.328 - 9.76\times10^{-2}\,S_p + 4.04\times10^{-4}S_p^2$,
$B = -\,6.913\times10^{-3} + 7.351\times10^{-4}\,S_p - 3.15\times10^{-6}\,S_p^2$,
$C = 9.6\times10^{-6} - 1.927\times10^{-6}\,S_p + 8.23\times10^{-9}\,S_p^2$,
$D = 2.5\times10^{-9} + 1.666\times10^{-9}\,S_p - 7.125\times10^{-12}\,S_p^2$, and
the validity of C_{psw} in (kJ/kg K) is for $273.15 < T < 453.15$ K, and $0 < S_p < 180$ g/kg, with accuracy of ± 0.28%.

♦ Seawater thermal conductivity, k_{sw}

The thermal conductivity, k_{sw} is an important property of seawater and one of the most difficult liquid properties to measure. Consequently data on seawater thermal conductivity is very limited. For aqueous solutions containing an electrolyte, such as seawater, the thermal conductivity usually decreases with an increase in the concentration of dissolved salts. The thermo-physical seawater thermal conductivity correlation is [26]

$$\log_{10}(k_{sw}) = \log_{10}(240 + 0.0002\,S_p) + 0.434 \left(2.3 - \frac{343.5 + 0.037\,S_p}{T + 273.15}\right)\left(1 - \frac{T + 273.15}{647 + 0.03\,S_p}\right)^{0.333} \text{ W/m K} \quad (32)$$

where the validity is for k_{sw} in W/m K, is for $0 < T < 180$ °C and $0 < S_p < 160$ g/kg, with accuracy of ± 3%.

♦ Seawater **dynamic viscosity, μ_{sw}**

The dynamic viscosity of seawater, μ_{sw} changes as a function of both temperature and salinity. The thermo-physical seawater dynamic viscosity correlation is [26]

$$\mu_{sw} = \mu_w\,(1 + A\,S_p + B\,S_p^2) \text{ kg/m s} \quad (33)$$

where:

$A = 1.541 + 1.998 \times 10^{-2}T - 9.52 \times 10^{-5}T^2$,
$B = 7.974 - 7.561 \times 10^{-2}T + 4.724 \times 10^{-4}T^2$,
$\mu_w = 4.2844 \times 10^{-5} + (0.157\,(T + 64.993)^2 - 91.296)^{-1}$, and
the validity is for μ_{sw} and μ_w in (kg/m.s) for $0 < T < 180$ °C and $0 < S_p < 0.15$ kg/kg, with accuracy: ± 1.5%.

3.5 The Effect of Condenser Performance on the Thermal Performance of the Plant

The present model studies the effect of the condenser efficiency, η_c on the exhaust steam temperature and pressure, condenser loss factor (LF), and output power and thermal efficiency of the power plant. The condenser loss factor is defined as the ratio of the heat released by the steam entering the condenser to the heat gained by its cooling water. The loss factor, output power and thermal efficiency are related to the condenser efficiency, η_c as [27].

$$\eta_c = \left(\frac{(T_{cwo} - T_{cwi})}{(T_c - T_{cwi})}\right) \% \qquad (34)$$

$$LF = \left(\frac{Q_{Rej,st}}{Q_{Rej,cw}}\right) \qquad (35)$$

$$LF = \left(\frac{(\dot{m}_{mix} * h_{in}) - (\dot{m}_{fw} * h_{out})}{\dot{m}_{CW} * C * \Delta T}\right) \qquad (36)$$

where $Q_{Rej,st}$= heat rejected from condensate steam, kW, $Q_{Rej,cw}$= heat rejected from condensate steam to cooling water, kW, $\dot{m}_{mix}$= mass flow rate of mixture inlet to condenser, kg/s, $\dot{m}_{fw}$= mass flow rate of feed water outlet from condenser, kg/s, $\dot{m}_{CW}$= mass flow rate of cooling water inlet to condenser, kg/s, h_{in}= enthalpy of mixture inlet to condenser, kJ/kg, and h_{out}= enthalpy of feed water outlet from condenser, kJ/kg.

4. Results and Discussion

4.1 Thermodynamic Data and State Diagrams of Plant Components

Classical thermodynamic heat balance calculations are performed using computer software engineering equation solver (EES) to determine the thermodynamic properties at inlet and exit of each component in the steam cycle of the assigned BWR NPP. Thus, it will be easy to calculate and quantify all key parameters which indicate the state of the plant such as heat added to steam, heat rejection, turbine output power, and the overall thermal efficiency.

These analyses represent the base to evaluate the impact of climate changes on the thermal performance of the proposed BWR plant. Figure 2 represents the designed heat balance model of the proposed plant at a cooling water temperature of about 5 °C, as obtained from the computer software Probera [28].

Figure 3 illustrates the simplified design heat balance model of the proposed plant at a cooling water temperature of about 5 °C, as created by EES.

Table 2 summarizes the inlet and exit thermodynamic properties for each component in the cycle of the O3 NPP at design conditions.

Figure 4 shows the thermodynamic state of each point and heat balance analysis of the studied plant on the T-s and h-s diagrams of the steam Rankine cycle.

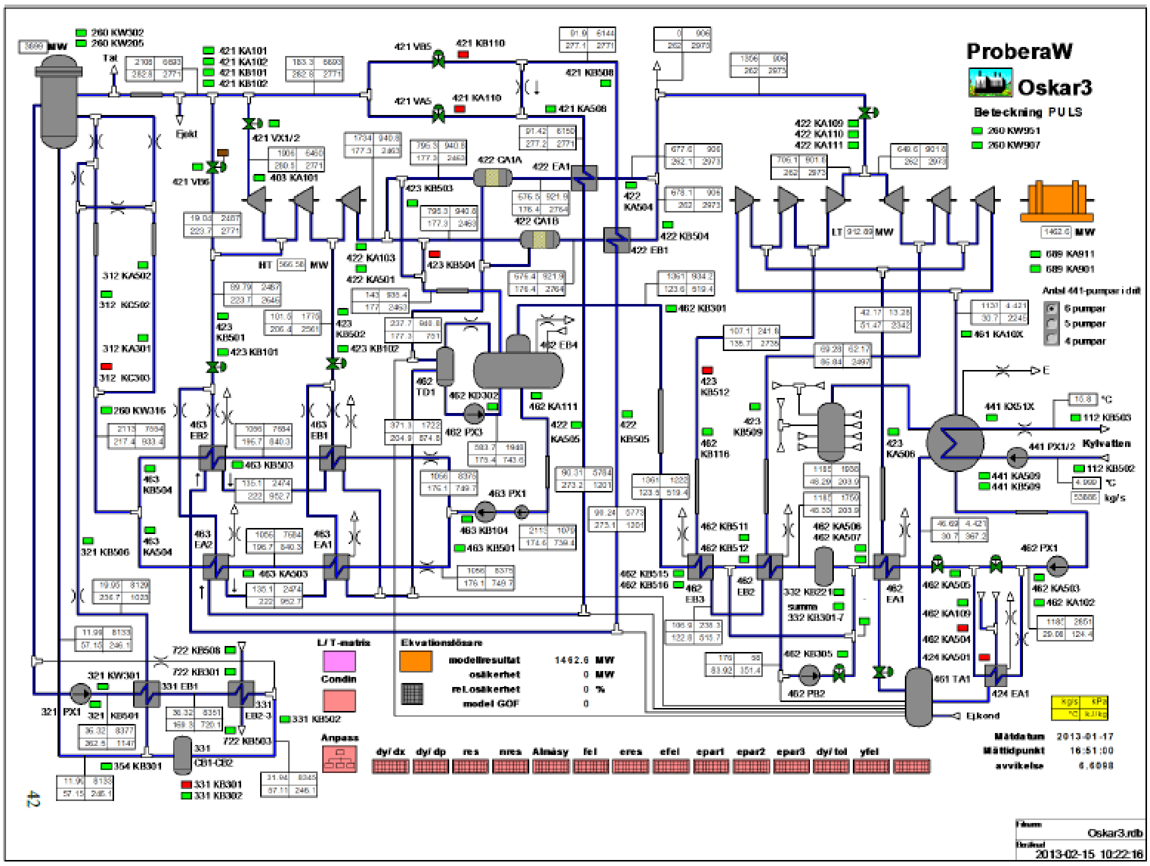

Figure 2. Approximation of the heat balance of the O3 plant at a cooling water temperature of about 5 °C

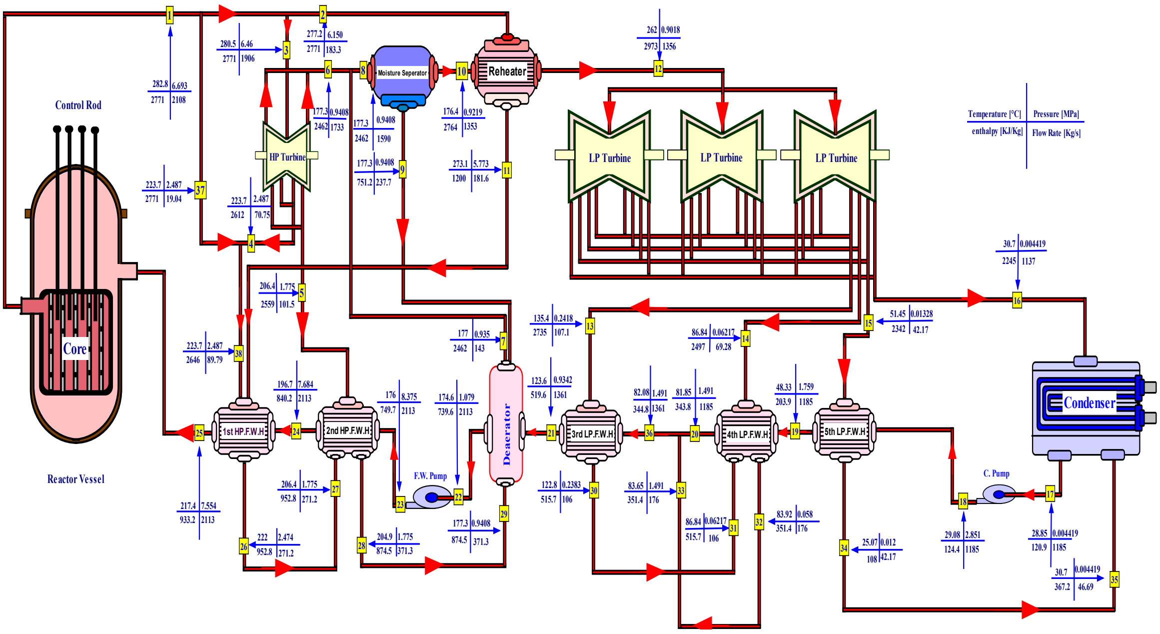

Figure 3. The EES model equivalent of thermodynamic and heat balance analyses for the proposed O3 BWR NPP

Table 2. Thermodynamic data of the plant

Point No.	Temperature, T (°C)	Pressure, p (MPa)	Enthalpy, h (kg/kJ)	Entropy, s (kJ/kg K)	Quality, X	Mass flow rate, (kg/s)
1	282.8	6.693	2771	5.827	0.997	2108
2	277.2	6.15	2771	5.857	0.9929	183.3
3	280.5	6.46	2771	5.84	0.9952	1906
4	223.7	2.487	2612	5.876	0.8968	70.75
5	206.4	1.775	2559	5.888	0.8759	101.5
6	177.3	0.9408	2462	5.912	0.8453	1733
7	177	0.935	2462	5.914	0.8455	143
8	177.3	0.9408	2462	5.912	0.8453	1590
9	177.3	0.9408	751.2	2.113	0	237.7
10	176.4	0.9219	2764	6.592	0.995	1353
11	273.1	5.773	1200	3.004	0	181.6
12	262.5	0.9018	2973	7.028	100	1356
13	135.4	0.2418	2735	7.112	100	107.1
14	86.84	0.06217	2497	7.083	0.9314	69.28
15	51.45	0.01328	2342	7.274	0.8941	42.17
16	30.7	0.004419	2245	7.411	0.8716	1137
17	28.85	0.004419	120.9	0.4206	−100	1185
18	29.08	2.851	124.4	0.4229	−100	1185
19	48.33	1.759	203.9	0.6813	−100	1185
20	81.85	1.491	343.8	1.096	−100	1185
21	123.6	0.9342	519.6	1.566	−100	1361
22	174.6	1.079	739.6	2.087	−100	2113
23	176	8.375	749.7	2.091	−100	2113
24	196.7	7.684	840.2	2.29	−100	2113
25	217.4	7.554	933.2	2.484	−100	2113
26	222	2.474	952.8	2.536	−100	271.2
27	206.4	1.775	952.8	2.54	0.03722	271.2
28	204.9	1.775	874.5	2.377	−100	371.3
29	177.3	0.9408	874.5	2.387	0.06094	371.3
30	122.8	0.2383	515.7	1.558	−100	106
31	86.84	0.06217	515.7	1.578	0.06639	106
32	83.92	0.058	351.4	1.122	−100	176
33	83.65	1.491	351.4	1.117	−100	176
34	25.77	0.012	108	0.3778	−100	42.17
35	30.71	0.004421	367.2	1.231	0.09826	46.96
36	82.08	1.491	344.8	1.099	−100	1361
37	223.7	2.487	2771	6.196	0.9832	19.04
38	223.7	2.487	2646	5.944	0.9152	89.79

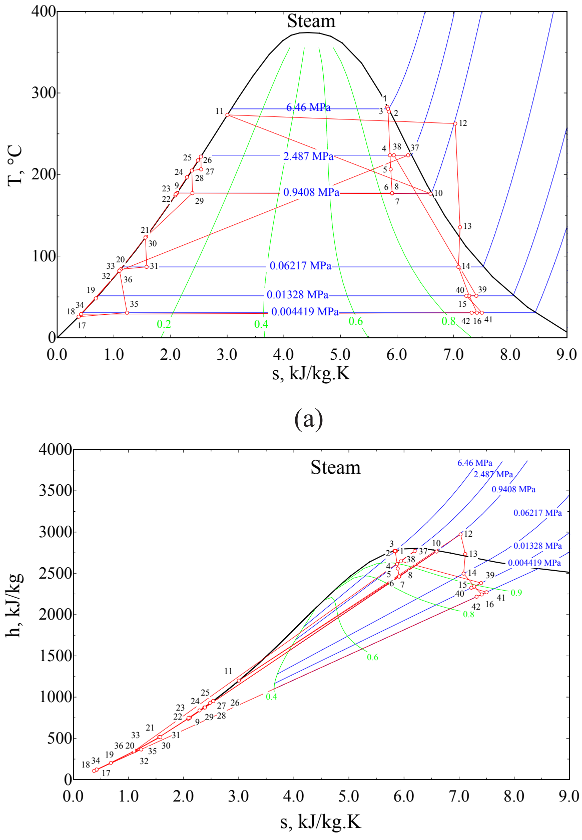

(a)

(b)

Figure 4. (a) T- s diagram and (b) h-s diagram of the O3 BWR NPP

4.2 The Effect of Condenser Inlet Cooling Water Temperature on $\dot{W}_{net}$ and η_{th}

The results show that as T_{cwi} increases both $T_{cwe,}$ and T_C increase. The relation between T_{cwe} and T_{cwi} is found to be linear, since the temperature difference ($T_{cwe}-T_{cwi}$) is constant with nil effect of the condenser terminal temperature difference TTD_C (T_C-T_{cwe}). Also, the variation of T_C and T_{cwi} exhibits a linear relationship, with approximately 1 °C difference in T_C for subsequent values of TTD_C at any constant value of T_{cwi}.

Variations of P_C, corresponding to the saturation temperature T_C, with T_{cwi}, resulted in increases in P_C of 0.000259 MPa, 0.000530 MPa, 0.001429 MPa, and 0.003242 MPa, for increases in of 1 °C, 2 °C, 5 °C, and 10 °C, respectively.

When P_C increases, the enthalpy of the extracted steam from low pressure turbines also increases and consequently the output power of turbines decreases. Figure 5 depicts the variation of $\dot{W}_{net}$ with T_{cwi}. It is clearly seen that $\dot{W}_{net}$ decreases as T_{cwi} increases. A decrease in $\dot{W}_{net}$ by 0.4123%, 0.8247%, 2.0618%, and 4.1927% are the result of increases in T_{cwi} of 1 °C, 2 °C, 5 °C, and 10 °C, respectively.

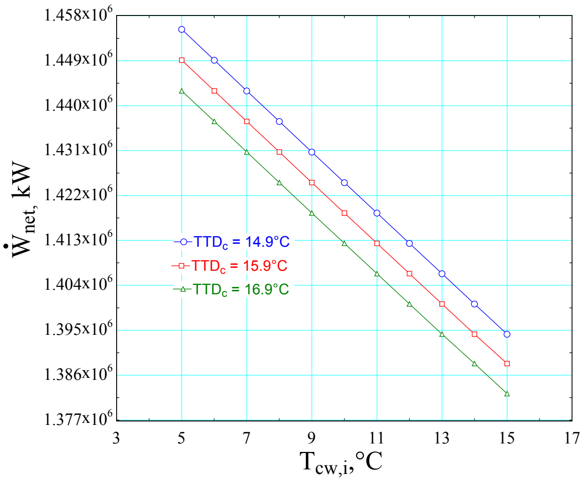

Figure 5. Relation between $\dot{W}_{net}$, and T_{cwi}

Figure 6 presents the variation of η_{th} with T_{cwi}. As shown, η_{th} decreases as T_{cwi} increases. Decreases in η_{th} by 0.16%, 0.32%, 0.8%, and 1.58%, are due to increases in T_{cwi} of 1 °C, 2 °C, 5 °C, and 10 °C, respectively.

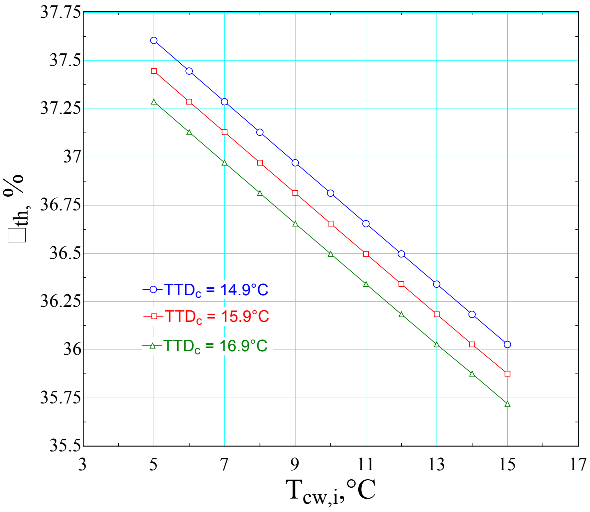

Figure 6. Relation between η_{th} and T_{cwi}

Figure 7 is a summary of the negative impact of variations in T_{cwi} on η_{th} and $\dot{W}_{net}$ of the plant.

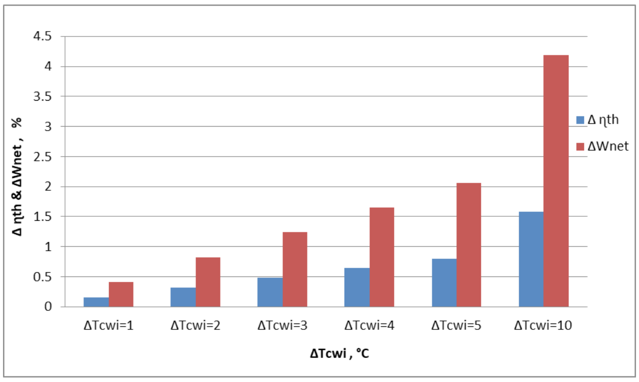

Figure 7. The impact of T_{cwi} on $\dot{W}_{net}$ and η_{th} of the O3 NPP

4.3 The Effect of Condenser Cooling Water Fouling on $\dot{W}_{net}$ and η_{th}

Many factors are affected by changes in T_{cwi} and F_i, such as the inside overall heat transfer coefficient $U_{i,}$ the outside overall heat transfer coefficient U_o, the condenser temperature T_C, and the condenser vacuum pressure P_C.

It is found that U_i and U_o decrease with increase in F_i and decrease in T_{cwi}. U_i decreases by 24 W/m^{2}K, and 200.4 W/m^{2}K for increases in F_i of 0.00002 m^{2}K/W, and 0.0002 m^{2}K/W, respectively for constant T_{cwi}. U_o decreases by 22.4 W/m^{2}K, and 185.7 W/m^{2}K as F_i increases by 0.00002 m^{2}K/W, and 0.0002 m^{2}K/W, respectively for constant T_{cwi}. These are significant decreases in U_i and $U_{o.}$

T_C increased by 0.3 °C and 3 °C for F_i increases of 0.00002 W/m^{2}K, and 0.0002 W/m^{2}K, respectively for constant T_{cwi}. P_C went up to 0.000076 MPa and 0.000816 MPa as F_i increased by 0.00002 m^{2}K/W, and 0.0002 m^{2}K/W, respectively for fixed T_{cwi}.

Figure 8 represents the relation between $\dot{W}_{net}$ and F_i for different values of T_{cwi}. It is observed that $\dot{W}_{net}$ decreases as F_i and T_{cwi} increase. $\dot{W}_{net}$ decreases by 0.1374% and 1.2371% of the nominal power due to increases in F_i by 0.00002 m^{2}K/W, and 0.0002 m^{2}K/W, respectively for fixed T_{cwi}.

Figure 9 indicates changes in η_{th} with F_i for different values of T_{cwi}. The results show a decrease in η_{th} by 0.05% and 0.48% due to increases in F_i of 0.00002 m^{2}K/W, and 0.0002 m^{2}K/W, respectively at constant T_{cwi}.

Any increase in F_i and T_{cwi} leads to increasing the fouling thermal resistance of the condenser and these lead to a reduction in U_i and U_o. These decreases in the overall heat transfer coefficients cause a decrease in the amount of the heat transferred to the seawater coolant, thus the steam turbine exhaust temperature increases and accordingly the corresponding pressure, which is a power loss.

Figure 10 shows a summary of the effect of F_i on $\dot{W}_{net}$ and η_{th} of the proposed NPP for a constant value of T_{cwi}.

The combined effect of condenser cooling seawater fouling and temperature on, $\dot{W}_{net}$ and η_{th} of the O3 plant are exhibited in Figure 11.

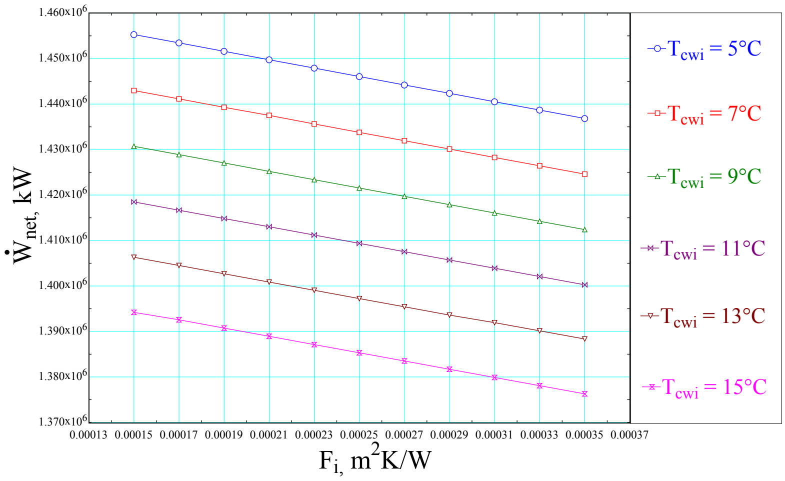

Figure 8. Variations of $\dot{W}_{net}$ with F_i for different values of T_{cwi}

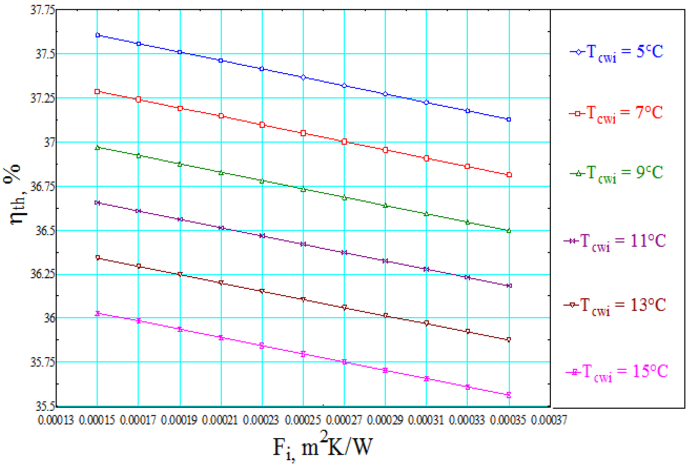

Figure 9. Variation of η_{th} with F_i for different values of T_{cwi}

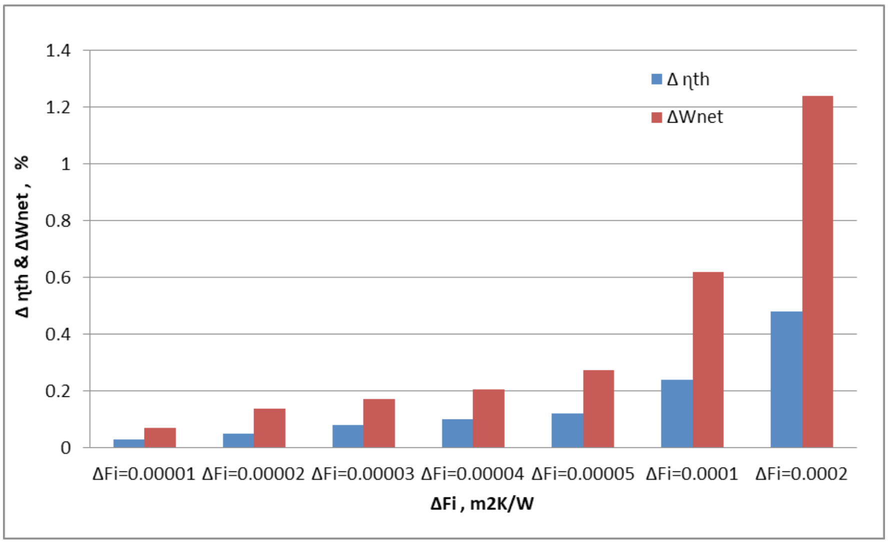

Figure 10. The effect of F_i on the thermal efficiency and output power of the BWR NPP

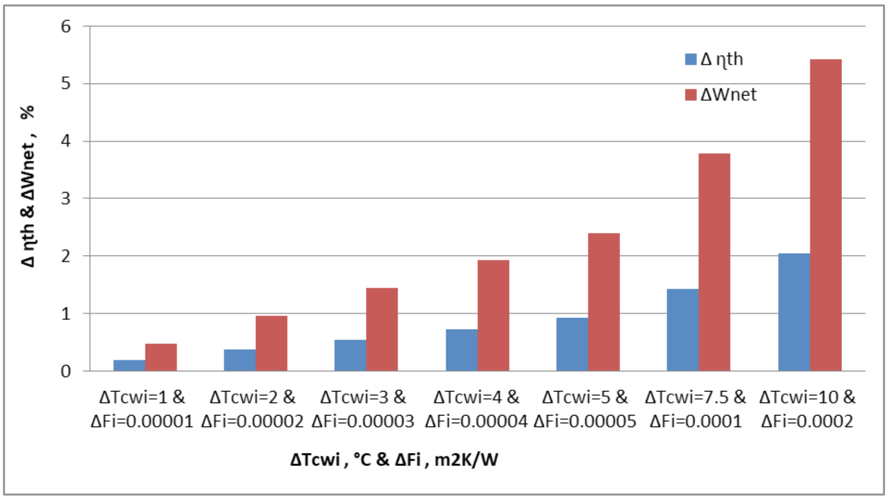

Figure 11. Impact of T_{cwi} and F_i on $\dot{W}_{net}$ and η_{th} of the NPP

4.4 The Effect of Condenser Cooling Water Salinity on $\dot{W}_{net}$ and η_{th}

The model demonstrates that the seawater density ρ_{sw} increases as S_P increases, and decreases with T_{cwi} increase. ρ_{sw} increases by 8 kg/m^3 and 79 kg/m^3 as S_p increases by 10 g/kg, and 100 g/kg, respectively for constant T_{cwi}.

The results depict that the seawater specific heat, $C_{P,sw}$ decreases with S_P and T_{cwi} increases until the salinity reaches 20%, thereafter the increase in S_P damps out this decrease and the effect of temperature takes over, i.e., $C_{P,sw}$ increases with increasing T_{cwi}. It is depicted that $C_{P,sw}$ decreases by 0.063 kJ/kg.K and 0.525 kJ/kg.K for S_p increases of 10 g/kg, and 100 g/kg, respectively at the same T_{cwi}.

The results give that μ_{sw} increases for S_P increase, and decreases as T_{cwi} increases. μ_{sw} increases by 0.000026 kg/m.s and 0.000364 kg/m.s for increases in S_p of 10 g/kg, and 100 g/kg, respectively for unchanged T_{cwi}.

The results revealed that the seawater thermal conductivity k_{sw} decreases as S_P increase, and increases with T_{cwi} increase. k_{sw} decreases by 0.0006 W/m.K and 0.0058 W/m.K, as S_p increases by 10 g/kg, and 100 g/kg, respectively at constant T_{cwi}.

Thermal resistance and heat transfer coefficients of the condenser change with changes in all the above mentioned thermo-physical properties of the condenser cooling seawater. The inside tube heat transfer coefficient of the condenser h_i decreases as S_P increases, and increases with increase in T_{cwi}. h_i decreases by 39 W/m^{2}K and 454 W/m^{2}K as S_p increases by 10 g/kg, and 100 g/kg, respectively for fixed T_{cwi}.

The change in h_i results in changing both U_i and U_o. In fact U_i and U_o, decrease as S_P increases, and increase as T_{cwi} increases. U_i and U_o decrease by 2 W/m^{2}K and 1.7 W/m^{2}K for a 10 g/kg increase in S_p, respectively, and by 21 W/m^{2}K and 19.1 W/m^{2}K, for S_p increase of 100 g/kg, respectively at constant T_{cwi}.

The decrease in overall heat transfer coefficients of the condenser reduces the output power and thermal efficiency of the plant. Figure 12 shows the relation between $\dot{W}_{net}$, and S_p, at different values of T_{cwi}. It is seen that $\dot{W}_{net}$ decreases as S_P and T_{cwi} increase. $\dot{W}_{net}$ decreases by about 0.0343% and 0.4123% of nominal power, for increases in S_p of 10 g/kg, and 100 g/kg, respectively for a given T_{cwi}.

Figure 13 exhibits the relation between η_{th}, and S_p, for some values of T_{cwi}. It is seen that η_{th} decreases approximately by 0.02% and 0.16%, as S_p increases by 10 g/kg, and 100 g/kg, respectively for the same T_{cwi}.

The adverse effects on hi, which lead to reductions in U_i and U_o are the result of the effects of increased seawater salinity on the thermo physical properties of the condenser coolant. This results in less capability of heat transfer to coolant. Accordingly, the turbine exhaust temperature and pressure increase, which truly reduces $\dot{W}_{net}$ and η_{th} of the plant.

The present results depict that changes in μ_{sw}, due to increases in S_P, produce the worst effect on $\dot{W}_{net}$ and η_{th} of the plant. ρ_{sw}, has the least effect on $\dot{W}_{net}$ and η_{th}. The results indicate that an increase in μ_{sw} from 0.001306 kg/m.s to 0.001627 kg/m.s, decreases $\dot{W}_{net}$ by about 2200 kW, and η_{th} by about 0.04%, while an increase in ρ_{sw} from 999.5 kg/m^3 to 1078 kg/m^3, decreases $\dot{W}_{net}$ by about 500 kW, and η_{th} by nearly 0.0125%.

Figure 14 represents the concluded results of the effect of S_p on $\dot{W}_{net}$ and η_{th} of the selected O3 NPP.

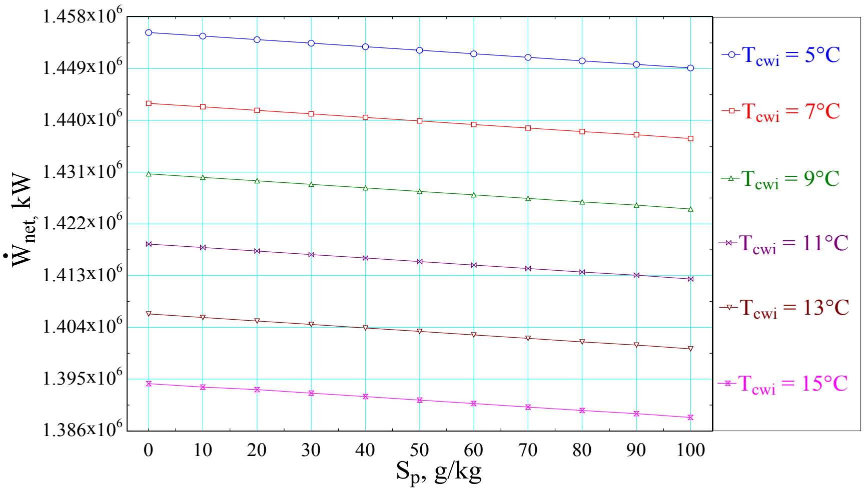

Figure 12. Variations of $\dot{W}_{net}$, with S_p for different values of T_{cwi}

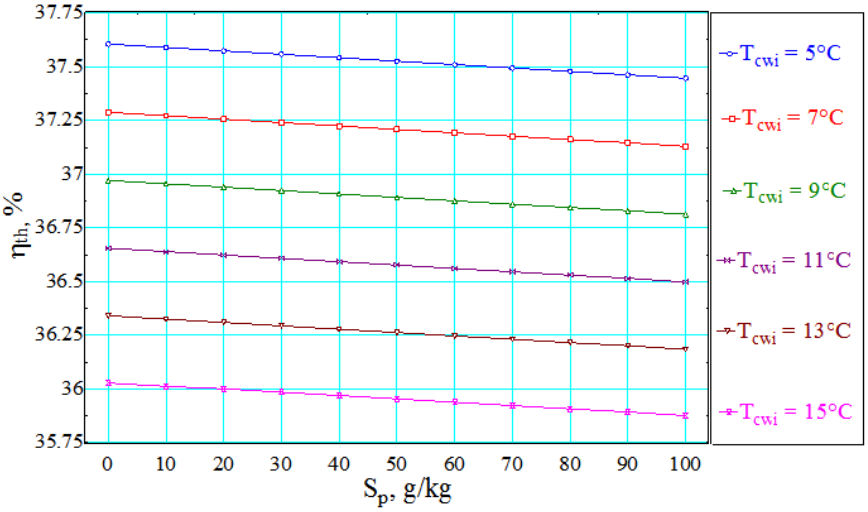

Figure 13. Variations of η_{th} with S_p for different values of T_{cwi}

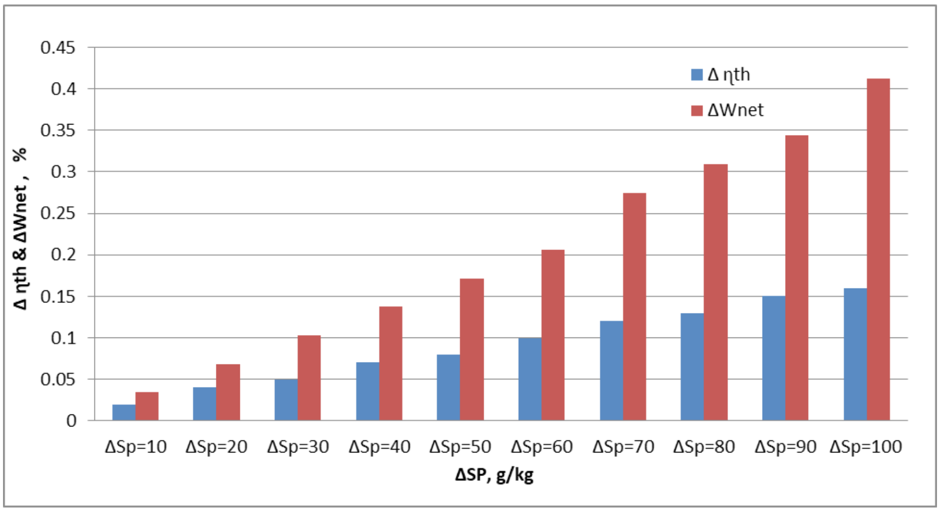

Figure 14. The Effect of S_p on η_{th} and $\dot{W}_{net}$ of the NPP

4.5 The Combined Effect of Condenser Cooling Water Temperature, Fouling Factor, and Salinity on $\dot{W}_{net}$ and η_{th}

The results indicate that U_i and U_o increase with increase in T_{cwi} and decrease with increasing F and Sp, whereas T_C, and P_C increase with increasing T_{cwi}, F, and S_p. For 1 °C increase in T_{cwi}, fouling factor of seawater and treated boiler feed water of 0.00002 m^2K/W and 0.00001 m^2K/W, respectively, and seawater salinity of 10 g/kg, cause decreases in: U_i, and U_o by 34 W/m^2K, 30.9 W/m^2K, respectively, and increases in T_C, and P_C by 1.44 °C and 0.000377 MPa, respectively. For an increase of T_{cwi} of 10 °C, fouling factor of seawater and treated boiler feed water by 0.0002 m^2K/W and 0.0001 m^2K/W, respectively, and S_p of 100 g/kg, U_i and U_o are reduced by 261.8 m^2K/W and 242 W/m^2K, respectively, and $T_{C,}$ and P_C increase by 14.4 °C and 0.004971 MPa, respectively.

The inside and outside overall heat transfer coefficients increase with temperature increase and decrease as fouling and salinity increase. The combined effect of increasing temperature, fouling, and salinity makes the thermal resistance of the condenser to go up; this explains the observed reductions in U_i and U_o. As a result, the pressure and temperature of the turbine exhaust are raised, which reduce both output power and thermal efficiency of the plant.

Figure 15 presents variations of $\dot{W}_{net}$ with T_{cwi} at different values of fouling factor of seawater F_i, fouling factor of treated boiler feed water $F_{o,}$ and S_p. It is seen that $\dot{W}_{net}$ decreases by 0.6185% of nominal power when increasing T_{cwi} by 1 °C, F_i and F_o by 0.00002 m^2K/W and 0.00001 m^2K/W, respectively and S_p by 10 g/kg. For an increase of T_{cwi} by 10 °C, F_i and F_o by 0.0002 m^2K/W and 0.0001 m^2K/W, respectively, and S_p by 100 g/kg, $\dot{W}_{net}$ decreases by 5.979% of nominal power. These are significant reductions which should be avoided.

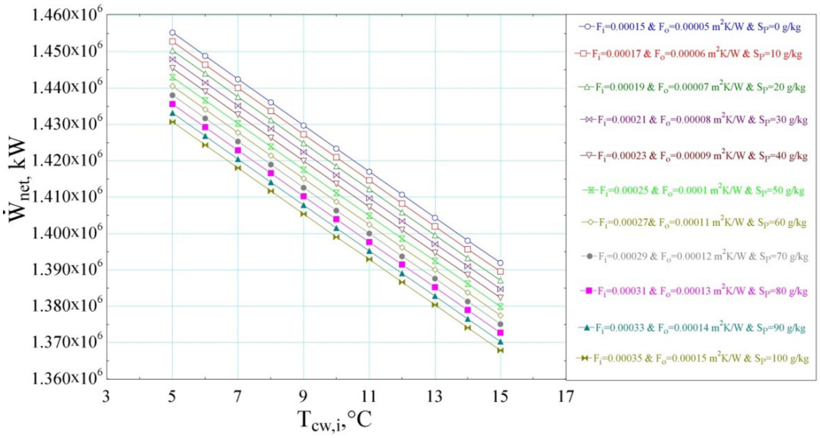

Figure 15. Variations of $\dot{W}_{net}$ T_{cwi} for different values of F_i, F_o and S_p

Figure 16 illustrates variations of η_{th} with T_{cwi} for different values of $F_{i,}$ $F_{o,}$ and S_p. As shown η_{th} decreases by 0.23% when increasing T_{cwi} by 1 °C, F_i and F_o by 0.00002 m^2K/W and 0.00001 m^2K/W, respectively, and S_p by 10 g/kg. For an increase of T_{cwi} by 10 °C, F_i and F_o by 0.0002 m^2K/W and 0.0001 m^2K/W, respectively, and S_p by 100 g/kg, η_{th} decreases by 2.26%. Such reductions cannot be ignored.

Figure 17 gives the combined impact of T_{cwi}, F_i, F_o, and S_p on both $\dot{W}_{net}$ and η_{th} of the NPP. Quite large losses in $\dot{W}_{net}$ and η_{th} can result from combined variations in condenser cooling sea water temperature, fouling and salinity. It is observed that $\dot{W}_{net}$ and η_{th} of the plant are reduced by 5.979% and 2.26%, respectively for extreme changes in T_{cwi}, F_i, F_o, and S_p.

4.6 The Effect of Condenser Performance on $\dot{W}_{net}$ and η_{th}

Since the condenser is a fundamental player in the thermal efficiency of power plants, therefore, we performed numerical calculations to obtain the effect of changing the condenser efficiency, η_C from 40% - 100 % on the condenser loss factor, LF, exhaust steam pressure, P_C and temperature, T_C, and plant $\dot{W}_{net}$, and η_{th}.

Figure 18 illustrates the effect of η_C on T_C and P_C. It is seen that T_C and P_C decrease with increasing η_C. For an increase in η_C from 40% - 100%, T_C decreases by about 16.2 °C and P_C decreases approximately by 0.002962 MPa.

The condenser loss factor is reduced as a result of the increase in the amount of heat transferred to the cooling seawater, which is a consequence of the decrease in the

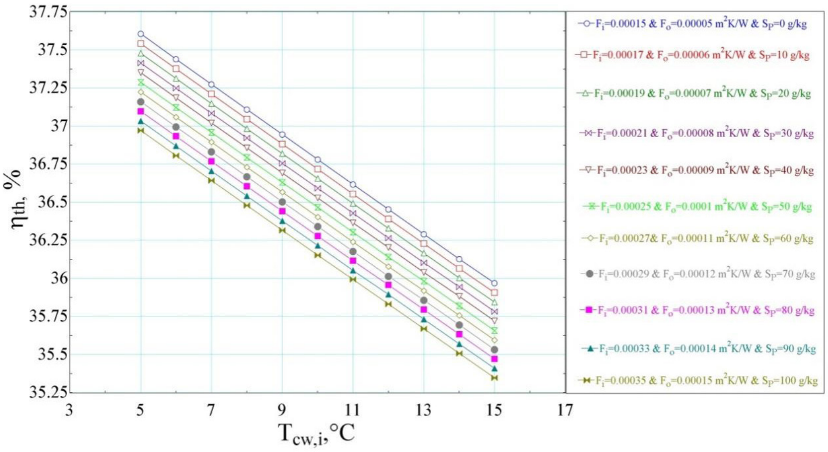

Figure 16. Variations of η_{th} with T_{cwi} at different values of F_i, $F_{o,}$ and S_p

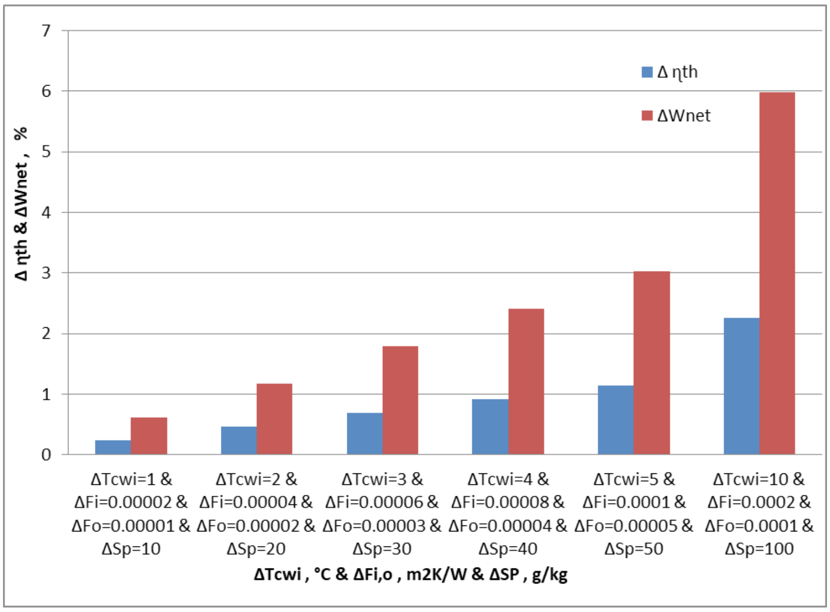

Figure 17. The combined effect of, T_{cwi}, F_i and F_{o} ,and, S_p on $\dot{W}_{net}$ and η_{th}

temperature of the turbine exhaust condensate. Figure 19 presents the effect of η_C, on LF. It is seen that LF decreases with increasing η_C. For an increase in η_C from 40% - 100%, LF decreases by about 0.009.

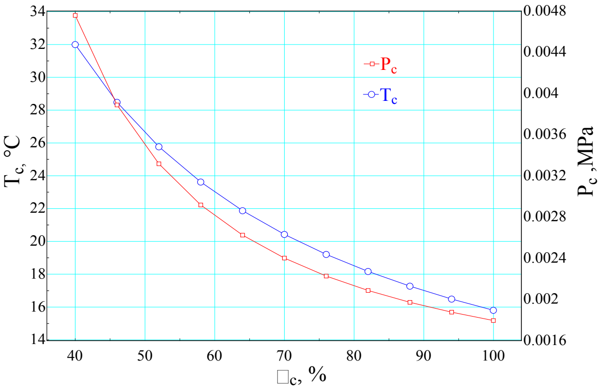

Figure 18. Variations of T_C and P_C, with η_C

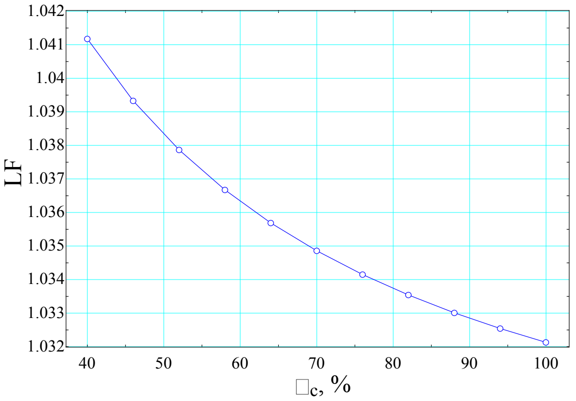

Figure 19. Variations of LF with η_C

The important conclusion is to determine quantitatively the effect of the condenser efficiency, η_C, on $\dot{W}_{net}$ and η_{th}, of the plant. It is clearly shown in Figure 20 that increasing η_C increases both $\dot{W}_{net}$ and η_{th}. For an increase in η_C from 40% - 100%, $\dot{W}_{net}$ increases by 102000 kW, i.e. by 7.049% of the nominal power, and η_{th} increases by 2.62%. These are high adverse effects and should be taken care of.

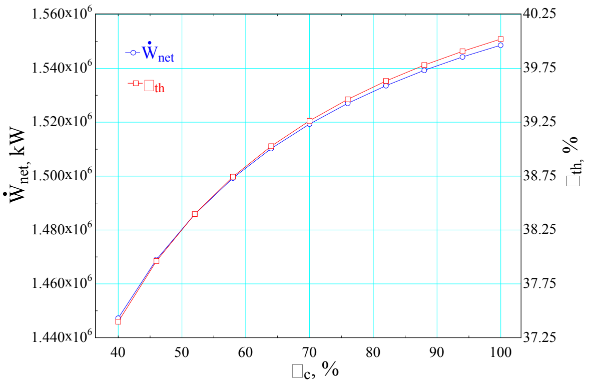

Figure 20. Variations of $\dot{W}_{net}$ and η_{th} with η_C

A decrease in η_C leads to increases in T_C, P_C, and LF. Increases in T_C and P_C translate directly to a power loss and hence less efficient plant. The role of the condenser, as a pivotal component in a power plant, cannot be overlooked. Inefficient condenser can be a burden on the plant. The optimum operating conditions of the condenser must be continuously maintained.

5. Conclusions

The main findings of this research are:

1) An increase of 1 °C in the temperature of the coolant extracted from the sea can result in decreases of 0.4123% and 0.16% in the power output and the thermal efficiency, respectively.

2) The output power and the thermal efficiency are reduced by 1.2371% and 0.48%, respectively for an increase in the fouling factor of the condenser cooling seawater of 0.0002 m^2K/W.

3) An increase in the condenser cooling seawater salinity of 100 g/kg, decreases the power output by approximately 0.4123%, and the overall thermal efficiency by about 0.16%.

4) The output power and the overall thermal efficiency are reduced by 5.979% and 2.26%, respectively, for combined extreme increases in the condenser cooling seawater temperature, fouling factor of seawater, fouling factor of treated boiler feed water, and salinity of 10 °C, 0.0002 m^2K/W, 0.0001 m^2K/W, and 100 g/kg, respectively.

5) A rise in the condenser efficiency from 40% to 100% increases the output power and thermal efficiency by 7.049%, and 2.62%, respectively. Thus, environmental factors and data should be used in the design of these condensers to compensate for the expected decrease in their performance under actual operating conditions during the life time of the NPP. The condenser design and its proper operation are rather important.

The highest adverse impact on the efficiency is due to increases in the condenser seawater cooling temperature, followed by fouling then salinity. Decreases in the thermal efficiency resulting from power losses are significant, and cannot be tolerated. Engineers are working hard and large investments are allocated in order to increase the efficiency by even 0.5% or 1%. The combined negative impacts of all considered factors together are likely to take place rather than their individual effects. Moreover, the extreme values could be achieved in the light, for instance of increased global climate impacts, increasing maritime trade, human activities, and increased water desalination.

The site of NPPs to be built on seas should be carefully selected, in order for changes in characteristics of seawater in the selected site to be a minimum. However, adverse impacts on the thermal performance of the plant are unavoidable as the operation time goes by, and these should be minimized or eliminated if at all possible. It is recommended to introduce an additional component in new NPPs to keep the seawater condenser coolant temperature, fouling, and salinity within design values. The temperature could be controlled by a heat exchanger working in connection with a refrigeration unit, or/and blow down of hot water and add cold fresh water. Fouling could be controlled chemically, mechanically or otherwise; it is the hardest to deal with. Salinity may be reduced chemically or/and by adding soft water. All could be controlled in one unit with specific sensors for each item, with automatic control operation. The cost of such additional component would be compensated by decreases of the high maintenance costs in NPPs, fuel cost, waste disposal, and keeping the plant operating within its rated efficiency.

The present conclusions should be useful in the design of NPPs in order to avoid the deterioration in the plant's efficiency, which has many adverse technical and economic implications.

Author Contributions

S. Ibrahim: Methodology, Validation, Visualization, Formal analysis, Writing - review & editing, Methodology, Conceptualization, Supervision, Project administration. I. Aggour: Data curation, Software, Methodology, Writing-original draft.

Conflict of Interest

The authors declare that they have no known competing financial interests or personal relationships that could have appeared to influence the work reported in this paper.

Funding

This research did not receive any specific grant from funding agencies in the public, commercial, or not-for-profit sectors.

References

[1] Ibrahim, S.M.A., Ibrahim, M.M.A., Attia, S.I., 2014. The impact of climate changes on the thermal performance of a proposed pressurized water reactor nuclear-power plant. International Journal of Nuclear Energy, Hindawi, Article ID 793908.

[2] Kim, B.K., Jeong, Y.H., 2013. High cooling water temperature effects on design and operation safety of nuclear power plants in the Gulf region. Nuclear Engineering and Technology. 45(7), 961-968.

[3] Durmaya, A., Sogut, O.S., 2006. Influence of cooling water on the efficiency of a pressurized water reactor nuclear power plant. International Journal of Energy Research. 30, 799-810.

[4] Linnerud, K., Mideksa, T.K., Eskeland, G.S., 2011. The impact of climate change on nuclear power supply. The Energy Journal. 32, 149-168.

[5] Darmawan, N., Yuwono, T., 2019. Effect of increasing seawater temperature on performance of steam turbine of Muara Tawar power plant. The Journal for Technology and Science. 30(2), 60-63.

[6] Pattanayak, L., Padhi, B.N., Kodamasingh, B., 2019. Thermal performance assessment of steam surface condenser. Case Studies in Thermal Engineering. 14.

[7] Prada, S.S., Manichandra, M.G., et al., 2018. Experimental study on performance of steam condenser in 600 MW Singareni thermal power plant. International Journal of Mechanical Engineering and Technology (IJMET). 9(3), 1095-1106.

[8] Alus, M., Elrawenu, M., Kawan, F., 2017. The effect of the condenser inlet water Temperature on the combined cycle power plant performance. World Wide Journal of Multidisciplinary Research and Development. 3(10), 206-211.

[9] Khan, A.H., Islam, Md.S., 2019. Prediction of thermal efficiency loss in nuclear power Plants due to weather conditions in tropical region. Energy Procedia. 160, 84-91.

[10] Ibrahim, S.M.A., Attia, S.I., 2015. The influence of condenser cooling seawater fouling on the thermal performance of a nuclear power plant. Progress in Nuclear Energy. 76, 421-430.

[11] Alabrudzinski, S., Markuwski, M., Trafczynski, M., et al., 2016. The influence of fouling build-up in condenser tubes on power generated by a condensing turbine. Chemical Engineering Transactions. 52, 1225-1230.

[12] Qureshi, B.A., Zubair, S.M., 2005. The impact of fouling on performance evaluation of evaporative coolers and condensers. International Journal Energy Research. 29(14), 1313-1330.

[13] Muller-Steinhagen, H., 1999. Cooling water fouling in heat exchangers. Advances in Heat Transfer. 11, 415-496.

[14] Bott, T.R., 1995. The design, installation, commissioning and operation of heat exchangers tominimize fouling. Fouling of Heat Exchangers, Chapter 13, Chemical Engineering Monographs. 26, 269-286.

[15] Gautam, R.K., Parar, N.S., Vyas, B.G., 2017. Effect of fouling on thermal hydraulic Parameter of shell and tube heat exchanger. Student Conference, Czech Technical University, Prague, Czech Republic.

[16] Ur-Rehman, K.J., Qureshi, B.A., Zubair, S.M., 1994. A comprehensive design and Performance evaluation study of counter flow wet cooling towers. International Journal of Refrigeration. 27, 914-923.

[17] Satpathy, K.K., Mohanty, A.K., Sahu, G., et al., 2010. Biofouling and its control in seawater cooled power plant cooling water system - A review. Nuclear Power. Pavel Tsvetkov (Ed.).

[18] Ibrahim, S.M.A., Attia, S.I., 2015. The influence of the condenser cooling seawater salinity changes on the thermal performance of a nuclear power plant. Progress in Nuclear Energy. 79, 115-126.

[19] Wiesenburg, D.A., Brenda, J.L., 1989. A synopsis of the chemical/physical properties of Seawater. Ocean Physics and Engineering. 12(3&4), 127-165.

[20] Ibrahim, M.M.A., Badawy, M.R., 2014. A parametric study of the impact of the cooling water site specific conditions on the efficiency of a pressurized water nuclear power plant. International Journal of Nuclear Energy. Article ID 569658.

[21] Sharqawy, M.H., Hussin, I.S., Zubair, S.M., et al., 2011. Thermal evaluation of seawater cooling tower. Proc. of the ASME 2011 Int. Mechanical Engineering Congress and Exposition. pp. 1-8. Denvor, Colorado.

[22] Taku, N., Jiao, I., et al., 2014. Effects of salinity on heat transfer coefficient of forced convective single phase seawater flow. Int. Workshop on Nuclear Safety and Sever Accident (NUSSA), Kashimo, Japan.

[23] Ibrahim, S.M.A., Attia, S.I., 2015. The combined effect of changes in the condenser cooling seawater temperature, fouling and salinity on the thermal performance of pressurized water reactor nuclear power plant. International Journal of Nuclear Energy Science & Technology. 9(1).

[24] Kronblad, R., 2013. Oskarshamn 3 - optimization after power update. Lund University.

[25] Holman, J.P., 2010. Heat Transfer. 10th Edition. McGraw-Hill.

[26] Sharqawy, M.H., Lienhard, V.J.H., Zubair, S.M., 2010. Thermo physical properties of seawater; Are-view of existing correlations and data. Desalination and Water Treatment. 16, 354-380.

[27] Dutta, A., Das, A.K., Chakrabaru, S., 2014. Study on the effect of cooling water temperature rise on loss factor and efficiency of a condenser for a 210 MW thermal power unit. International Journal of Engineering Technology and Advanced Engineering. 3(3), 485-489.

[28] Garland, Wm. J., 2014. The essential CANDU: A textbook on the CANDU nuclear power plant Technology. Department of Engineering Physics, McMaster University, Canada.

Nomenclature

A	Heat transfer area	m^2
C	Specific heat	kJ/kg K
d	Diameter	m
F	Fouling factor	m^2K/W
g	Acceleration of gravity	m/s^2
L	Length	m
LF	Loss factor	Dimensionless
LMTD	Log mean temperature difference	°C
h	Enthalpy	kJ/kg
k	Thermal Conductivity	W/m K
$\dot{m}$	Mass flow rate	kg/s
N	Number	Dimensionless
Nu	Nusselt number	Dimensionless
P	Pressure	bar
Pr	Prandtle number	Dimensionless
Q	Heat	kJ/kg
R	Resistance	m^2K/W
r	Radius	m
R	Reynolds number	Dimensionless
s	Entropy	kJ/kg K
S_P	Salinity	g/kg
T	Temperature	°C
ΔT	Temperature difference	°C
U	Overall heat transfer coefficient	W/m^2K
V	Flow velocity	m/s
W	Output power	kJ/kg
X	Moisture content	Dimensionless

Greek Letters

η	Efficiency	%
ρ	Density	kg/m^3
μ	Dynamic viscosity	kg/m.s

Subscripts

ad	Added
c	Condenser
cp	Condensate pump
cw	Cooling water
cwi	Cooling water in
cwo	Cooling water out
f	Reheated steam
h	Horizontal
fw	Feed water
fwp	Feed water pump
HPT	High pressure turbine

i, in	Inside
LPT	Low pressure turbine
mix	Mixture
net	Net
o, out	Outside
P	Pump
p	Specific
r	Reheat
rej	Rejected
s	Drained water
st	Steam
T	Turbine
th	Thermal
v	Vapor
w	Tube wall

Abbreviations

BWR	Boiling water reactor
BPV	Bypass valve
FWH	Feed water heater
HP	High pressure
HPFWH	High pressure feed water heater
HPST	High pressure steam turbine
LPFWH	Low pressure feed water heater
LPST	Low pressure steam turbine
NPP	Nuclear power plant

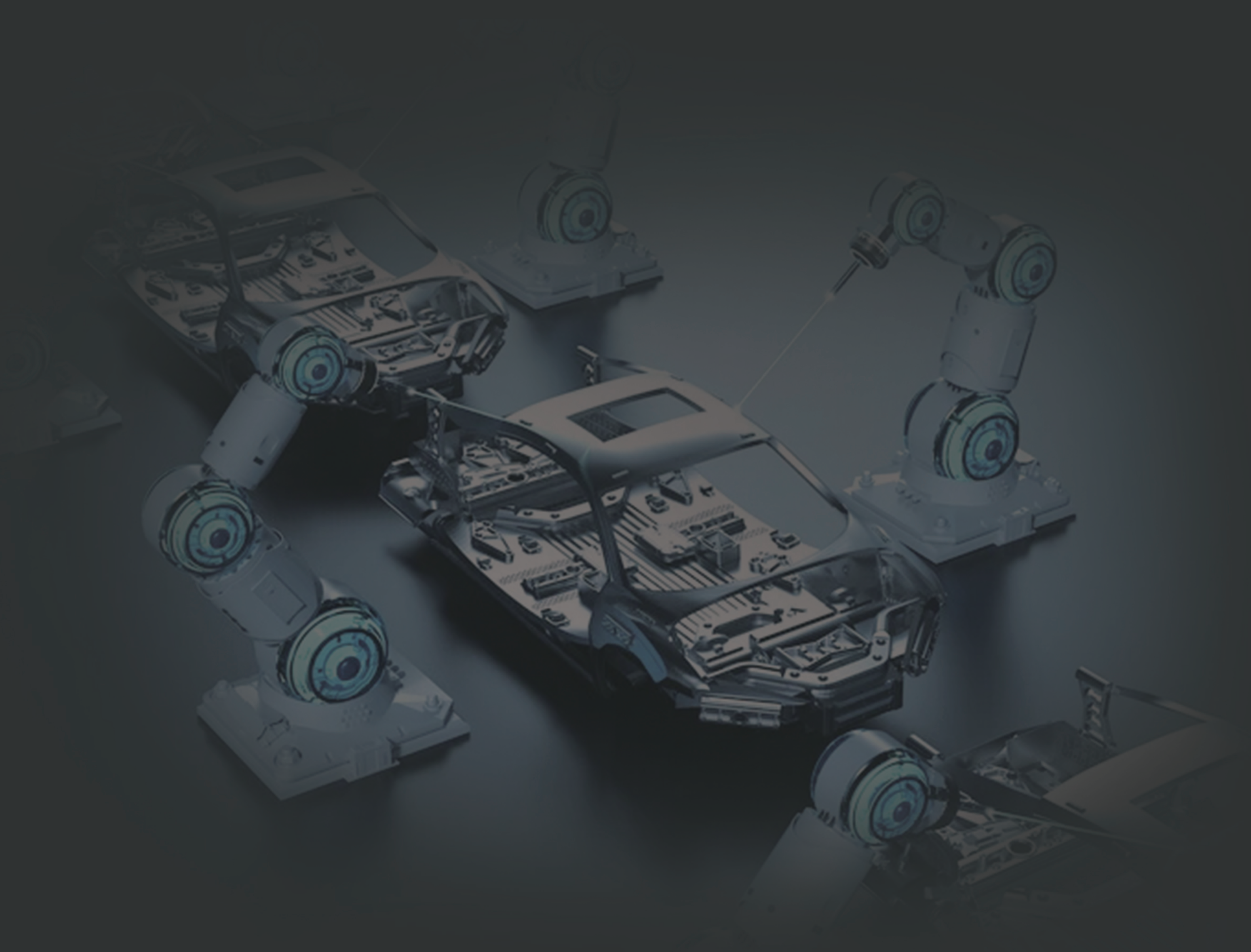

BILINGUAL
PUBLISHING CO.
Pioneer of Global Academics Since 1984

Tel:+65 65881289
E-mail: contact@bilpublishing.com
Website:ojs.bilpublishing.com

2810-935X
01
9 772810 935223